FEM Based Analysis of High Pass Birdcage Resonators for B1 Field Mapping

by

Shirish S. Karveer

A thesis
Presented to Lakehead University
in partial fulfillment of the requirements for the degree of
Master of Science in Electrical and Computer Engineering

Thunder Bay, Ontario, Canada
2015

Abstract

3D full wave finite element method (FEM) based electromagnetic (EM) analysis is a technique to map EM fields generated by electrical devices. To better understand and apply this technique to magnetic resonance imaging (MRI) radio frequency (RF) birdcage resonators, a vast number of 3D full wave EM simulations are required for validation and optimization of the B1 field generated by them since they have to be tuned to a particular Larmor frequency.

In the past RF birdcage resonators were constructed without doing any 3D full wave EM analysis and more emphasis was laid on tuning and matching the electrical circuits used to make these resonators. However modeling birdcage resonators in a 3D computer aided engineering (CAE) simulation environment is important to observe the resonance behavior and the B1 field distribution inside the birdcage resonator volume before its construction thus saving valuable resources.

In this work we have attempted to map B1 field distribution inside the full and half birdcage resonators tuned to Larmor frequency for proton nuclei at 3 Tesla with the help of FEM. FEM essentially converts the problem of solving Maxwell's partial differential equations into solving a large system of linear equations. In this work we make use of the ANSYS high frequency structure simulator (HFSS) which is an FEM based frequency domain solver. The results of the full birdcage resonator are further compared with experimental outcomes. The phantoms used for experiments and simulation are both symmetric and non-symmetric ones.

It can be concluded that HFSS or similar FEM based EM simulator may be used to predict the B1 field inside loaded RF resonators to obtain information of the B1 field behavior. It is observed that B1 field distribution inside the birdcage resonator varies with different types of phantoms used to mimic small animals for MRI. B1 field maps and resonance results from simulation and experiment are presented. Finally this thesis concludes with areas of improvement and a road map for future work.

Acknowledgements

Firstly I would like to thank my supervisors Dr. Carlos Christoffersen and Dr. Laura Curiel for their support and guidance during my graduate studies.

I would also like to express my sincere appreciation to Dr. Krishnamoorthy Natarajan and Dr. Mitchell S. Albert for showing an interest in my work and serving on my thesis committee.

A very big thanks go to my colleagues. First to Mr. Chris Abraham for helping me with MRI scans and his birdcage resonator. Also to Mr. Peter Luong, Mr. Kristoffer Fedick, Mr. Ruiqi Song and Mr. Tao Li.

Thanks Mr. Jason Servais and Mr. Bruce Misner for allowing the use of electrical engineering labs and assistance in some measurements.

Thanks Dr. A Chen and Sapanbir Thind for allowing the use of Lakehead university chemistry lab to prepare saline solution used in this work.

Thanks CMC Microsystems for providing access to ANSYS – HFSS.

Thanks Faculty of Electrical and Computer Engineering for some funding and for the environment that encourages one and all to push beyond their learning boundaries.

Thanks to authors who influenced my thinking and their names are perhaps best suggested by the references.

And most importantly, I wish to thank my family, friends and co-workers for their support, patience and encouragement.

- *Shirish S. Karveer (2015)*

Table of Contents

List of Figures

List of Tables

List of Symbols

Symbol	Meaning
$\nabla\times$	Curl of
$\bar{E}$	Electric field intensity
$\bar{J}$	Source current density
ω	Angular frequency
γ	Gyromagnetic ratio
$\bar{H}$	Magnetic field intensity
B0	Main magnetic flux density
B1	Radio frequency magnetic flux density
$\bar{B}$	Magnetic flux density
μ	Magnetic moment
μ_0	Permeability of free space
M	Net magnetization

List of Abbreviations

Abbreviation	Meaning
FEM	Finite element method
MRI	Magnetic resonance imaging
MR	Magnetic resonance
RF	Radio frequency
HFSS	High frequency structure simulator
EM	Electromagnetic
CAE	Computer aided engineering
TBRRI	Thunder bay regional research institute
TEM	Transverse electromagnetic
SNR	Signal to noise ratio
NMR	Nuclear magnetic resonance
PDE	Partial differential Equation
RAM	Random access memory
RLC	Resistor, Inductor and Capacitor
TR	Repetition time
TE	Echo time
FOV	Field of view
ROI	Region of interest
VNA	Vector network analyzer
QUCS	Quite universal circuit simulator
FFE	Fast field echo (a type of pulse sequence)
ER	End ring
FDM	Finite difference method

Chapter 1
Introduction

1.1 Basics of MRI and its origin

Magnetic resonance imaging (MRI) is a medical imaging modality based on the nuclear magnetic resonance (NMR) phenomenon (NMR is defined as a physical phenomenon in which nuclei in a magnetic field absorb and emit electromagnetic radiation) that provides a means of obtaining detailed, high quality images for use by the medical community for diagnostic purposes. The difference between MRI and other imaging modalities like X-ray and Computed Tomography is that there is no ionizing radiation involved in MRI. MRI is a technique that depends on static and slowly changing magnetic fields and electromagnetic (EM) energy primarily in the high frequency through very-high-frequency bands to provide soft and hard tissue images with outstanding contrast that can be both static and dynamic in nature [1].

The phenomenon of NMR was first discovered by Purcell [2] and Bloch [3] in 1946. In 1973, Lauterbur [4] and Mansfield [5] developed the techniques to generate MR images of a subject from NMR signals using a Fourier Transform. Ever since then MRI has evolved as a modality of choice for radiologists throughout the globe. This non-invasive diagnostic imaging modality has the ability to provide tomographic images with anatomical and functional information of a region of interest (ROI). ROI is defined as the area of anatomy being scanned which is of particular importance in the MR image inside the human body.

1.2 Components of an MRI system

The components of MRI system include the primary magnet, gradient coils, RF resonator (as shown in Figure 1.1 and the computing system [1]. The computing system is comprised of the electronic components like the pulse generators, amplifiers, an RF receiver and a digitizer. The static magnetic field refers to the primary magnetic field (B0 field), which is generated by the

primary magnet and is described by the relation (B0 = μ_0 H). This B0 field is originally the magnetic flux density [1] that needs to be varied from point to point in a controllable fashion, which is achieved by employing the gradient coils as illustrated in Figure 1.1. The gradient coils generate gradient fields which vary linearly in a prescribed direction. In addition, one must also have a B1 field (the radiofrequency EM field generated by birdcage resonator), which needs to be uniform to generate high quality MR images. Hence the RF resonator is an essential component in the MRI system to generate the B1 field.

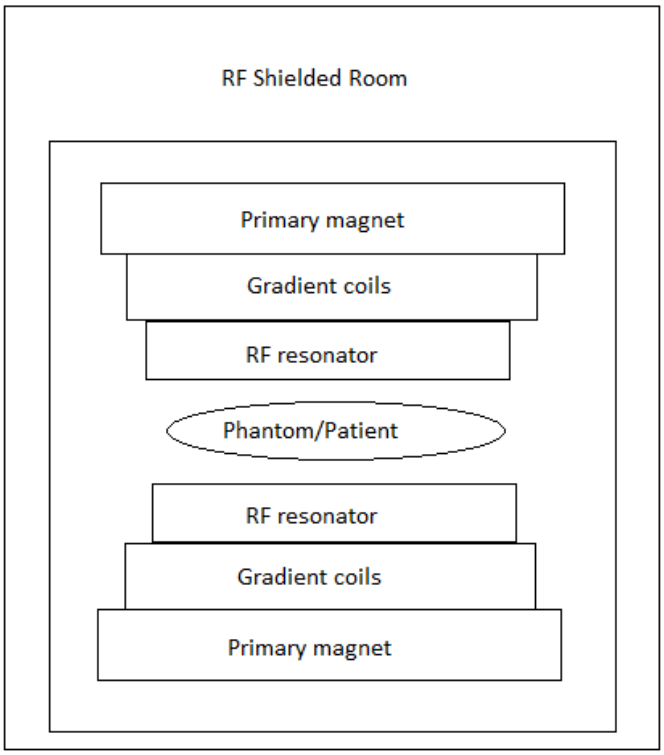

Figure 1.1 Components of MRI System [1]

1.3 RF resonators

RF resonators are one of the key components in MRI [6]. They are needed for two primary functions. One of them is to generate B1 field in the transverse plane in the ROI. This B1 field is perpendicular to B0 field and excites the nuclei (spins) in the object at the Larmor frequency (the frequency at which magnetic resonance in a nucleus is excited). The concept of Larmor frequency is described in Section 2.1. The other need for RF resonators is to receive signals transmitted by precession (precession is defined as slow gyration of the axis

of a spinning body so as to trace out a cone) of nuclear spins. These two functions are called excitation (transmission) and reception respectively.

RF resonators can be divided into three groups according to the needs they serve: transmit only, receive only and transmit/receive resonators. For the transmit RF resonators, it is desirable for them to generate a homogeneous B1 field in the volume of interest at the desired Larmor frequency. Providing good homogeneity along with low power consumption is highly preferable for the transmit resonators. Saddle resonators, TEM resonators and Birdcage resonators can be used as transmit resonators [8]. For the receive resonators, on the other hand, it is desired that they are able to receive signals with a high SNR, defined as the ratio between the amplitude of the received signal and background noise. Additionally, sensitivity, defined as ability of the resonator to pick up electrical signal, is required to be nearly uniform with respect to distance, inside the volume of the resonator [8].

In addition to above requirements given for RF transmit and receive resonators, there are other important requirements for the RF resonators such as having a good filling factor (the fraction of the resonator volume filled with phantom), quadrature excitation and reception capability. In this thesis, birdcage resonators, one of the most widely used RF resonator types in MRI and which have most of the requirements given above, are discussed in detail.

1.4 Motivation

To understand the EM field behavior inside the volume of birdcage resonators, numerous 2D and 3D full wave EM simulation studies have been conducted [7,8,9,10,11]. The main motivation is that with the help of these simulations it is possible to optimize the parameters of the birdcage resonator before construction, thus saving time and money. The parameters that can be optimized are geometry, permittivity, permeability and conductivities of materials. The solution frequency, input power, capacitance and inductance values can also be optimized. An example of geometry optimization is reduction in diameter size and/or length of the birdcage resonator which will directly have an impact on the costs related to copper strips and capacitors placed on the surface of birdcage resonator. The homogeneity of the B1 field needs to be

simulated and verified experimentally since it affects the MR image quality directly. Birdcage resonators are used for small animal MRI studies because the diameter of these resonators can be significantly reduced as per the size of the small animal. This means that the birdcage resonators can be constructed in such a way that the small animal fills most of the volume inside the birdcage resonator in order to exchange maximum electrical signal, as signal intensity will significantly reduce with an increase in distance [12]. Birdcage resonators also deliver sufficient B1 field homogeneity up to 14.1 Tesla for small animal experiments [12].

1.5 Objectives of this work

- Understand the working of the RF birdcage resonator and develop EM simulation models in Ansys HFSS [13]. (HFSS is a commercial finite element method (FEM) solver for electromagnetic structures from Ansys and FEM is a type of numerical method employed to map EM fields generated by any electrical device).
- Perform tuning of end ring capacitors for high pass birdcage resonator to achieve the desired resonance in Ansys HFSS.
- Understand the working of FEM as applied to EM simulation studies specifically for birdcage resonators.
- Extract and analyze the B1 field results inside a birdcage and a half birdcage resonator from HFSS EM simulations.
- Validate the B1 field simulation results with experimental outcomes for full birdcage resonator.
- Accelerate the birdcage and half birdcage resonator construction procedure by simultaneously improving their performance and reducing the prototyping costs associated with them using HFSS simulations.

1.6 Organization of this thesis

Chapter 2 presents the details relating to NMR physics, MRI concepts, review of relevant literature and previous studies on birdcage resonators. Chapter 2 also includes analysis of

birdcage resonators using lumped elements, practical considerations for designing a birdcage resonator and capacitance calculation along with the theory of FEM. Chapter 3 presents the design procedure of the full birdcage resonator in HFSS and mainly deals with the simulation and experimental results. Chapter 4 presents the design procedure of half birdcage resonator in HFSS and its simulation results. Last chapter mentions the conclusions and directs the future of this work.

Chapter 2
Background and Literature review

2.1 Nuclear Magnetic Resonance Imaging

Quantum mechanics reveals the existence of a property of atomic nuclei known as spin angular momentum which is defined as an intrinsic form of angular momentum carried by elementary particles, composite particles and atomic nuclei [7,14]. Spin angular momentum is the basis of the magnetic resonance phenomenon and hence MRI. MRI utilizes variations in the spin angular momentum of certain atomic nuclei that constitute biological structures to derive images that contain valuable information concerning the condition of the associated tissue. The variations in spin angular momentum result from interactions with an applied static magnetic field and EM radiation. The following explanation, equations and derivation are based on [7,14]. From a classical mechanics point of view, spin angular momentum can be thought of as originating from the motion of elementary charged particles that make up the nucleus of the atoms as they spin around their axis. Positive and negative charged particles can be regarded as spheres of distributed positive or negative charge, while neutral electrical particles such as the neutron can be thought of as a combination of distributed positive and negative charges. Since the particles that constitute the atom have mass, their rotation generates angular momentum. Moreover the motion of the distributed charge circulating around the axis of the particle will generate a small magnetic field. This magnetic field is called the magnetic moment. There exists a relationship between the angular momentum and the magnetic moment of the nucleus (a single proton). This relationship is given by:

$$\mu_z = \gamma \mathrm{J} \tag{2.1}$$

where μ_z = z-component of magnetic moment in $A.\mathrm{m}^2$, J = angular momentum in $\mathrm{Kg.m}^2/s$ and γ is gyromagnetic ratio (a characteristic constant of the given nucleus) in $\mathrm{Hz/T}$. The magnetic moment is a property of the given nucleus and it determines the sensitivity of MRI. Hydrogen nuclei, containing a single proton, possess the largest magnetic moment, which together with its high concentration in any biological tissue make it the nucleus of choice in

MRI. Consider the case of a single hydrogen nucleus in the presence of an applied static magnetic field, because of the interaction between the magnetic moment of the nucleus and the applied magnetic field, the nucleus will align itself with the applied field in one of two possible states: either with the field (the more probable low energy state also known as the parallel or spin up state) or against the field (the anti-parallel or spin down) state. This is shown in Figure 2.1. The energy difference between the two states is directly proportional to the strength of the applied magnetic field and is given by:

$$\Delta E = 2\mu_z B_0 \tag{2.2}$$

Where μ_z = z-component of the magnetic moment and B_0 = magnetic flux density of the applied static field. When the object to be imaged is placed in a static magnetic field H (or in terms of magnetic flux, $B_0 = \mu H$; where B_0 is usually called the 'primary magnetic field' in MRI language) a torque is experienced by magnetic moment which facilitates precession [1]. The application of an RF pulse with sufficient power (with a magnetic flux component) is called ' B_1 ' or called the ' B_1 field'.

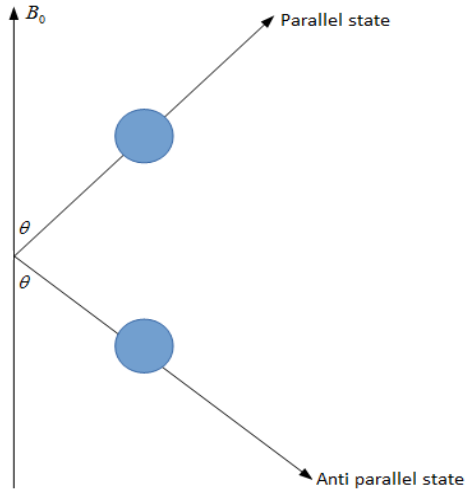

Figure 2.1: Orientation of a proton under the influence of a static magnetic field [8]

It is observed that μ_z does not align completely but with an angle, termed as Flip angle. This is shown in Figure 2.2. Nuclei can change from one state to another by absorbing or emitting photons with energy equal to the energy difference. From quantum theory, the frequency of these photons can be found using:

$$\Delta E = hf \tag{2.3}$$

where h is Planck's constant. By substituting Equation (2.3) in (2.2), the frequency 'f' of the photons can be determined using:

$$f = \frac{2\mu_z}{h} B_0 \tag{2.4}$$

Hence, for a given nucleus, the frequency is directly proportional to the flux density of the applied field. The effect of the applied field B_0 is the formation of a net magnetic moment along the z-axis and the precession of the nucleus about the z-axis. Larmor frequency is equal to the frequency of the emitted or absorbed photons as calculated in Equation (2.4). This frequency can be expressed in terms of the gyromagnetic ratio and is given by [8]:

$$f = \frac{\gamma}{2\pi} B_0 \tag{2.5}$$

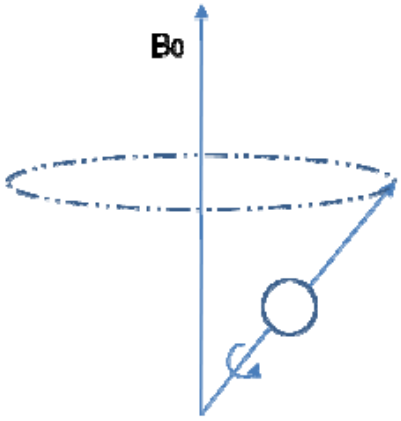

Figure 2.2: Precession of a proton about the axis of applied magnetic field [8]

The excitation and detection of an NMR signal is facilitated by the establishment of a resonance condition. The resonance condition represents a state of alternating absorption and dissipation of energy. Energy absorption is achieved through the application of RF pulses, while energy dissipation is caused by relaxation processes; both transverse and longitudinal relaxation. Consider the application of RF radiation at the Larmor frequency to a bulk sample of non-magnetic material in an applied static magnetic field. This is depicted in Figure 2.3. The applied RF signal is composed of coupled electric and magnetic field components. In Figure 2.3, B_1 resides in a plane perpendicular to B_0 and precesses about B_0 at the Larmor

frequency. Upon application of the RF pulse, the net magnetization M starts to rotate about the axis of B_1, since B_1 and M are rotating about B_0 at the Larmor frequency, they appear stationary relative to each other. This is also depicted in Figure 2.3. The purpose of the application of B_1 field is to rotate M by a certain angle away from the B_0 axis. It is expected for a birdcage resonator to exhibit uniform B_1 field inside it's volume. The percentage B_1 field homogeneity is defined using the following formula and its applicable results for this work are presented in Chapter 3.

$$Percentage\ B_1\ field\ homogeneity = \frac{Average\ normalized\ B_1\ field - Standard\ deviation}{Average\ normalized\ B_1 field} \times 100$$

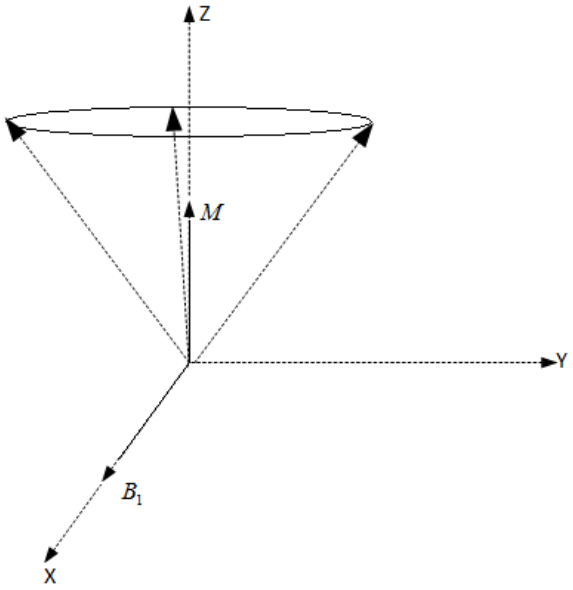

Figure 2.3: Precession of net magnetization M

2.1.1 Slice selection

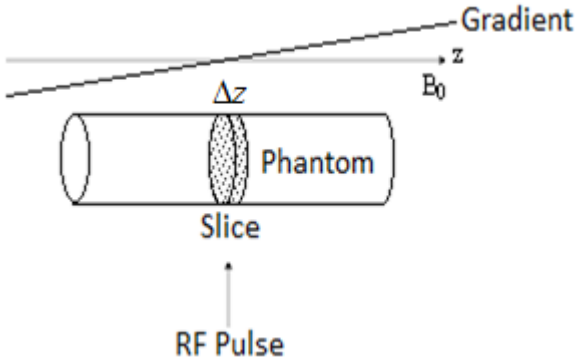

Figure 2.4 Slice selection

MRI is a technique that generates cross sectional images of human anatomy in a certain ROI and a fixed plane. This particular image in a certain plane is termed as a slice. So the first step to do an MRI, is to decide this particular slice to be imaged. It is known from [14] that Larmor frequency is proportional to the strength of magnetic field and the nuclei in a particular slice are excited by a specific Larmor frequency. Hence there arises a need to excite the nuclei, limited to only the slice of interest simultaneously keeping all other nuclei out of excitation, that is achieved with the help of gradient coils, which generate the gradient magnetic field. This gradient magnetic field along with the primary magnetic field B_0 in a specific combination make it possible to select the slice of interest, thus making way for an MR image.

2.1.2 Spatial encoding

Once the slice has been selectively excited after the application of RF pulse or B1 field, it is essential to identify from where within a particular slice each component of the signal is coming from [14]. Hence to generate an MR image the information needed is to know the amount of signal coming from each voxel which is termed as spatial encoding and is composed of frequency and phase encoding. The next thing is to know the procedure to get information about single voxels within the selected slice. The slice is selected using a selective RF pulse (generally 90^0 pulse) and then switching on the slice select gradient during the application of this pulse and then switching it off after application of this pulse. After this MRI scanner will send a RF refocusing pulse (generally a 180 degree pulse) and the gradient is switched on again

during application of this pulse. To obtain spatial information in the x-direction another gradient is applied termed as the frequency encoding gradient. In addition to this to obtain spatial information in y-direction one more gradient is applied which is termed as the phase encoding gradient. Hence it can be said that x-coordinate is a function of unique frequency and y-coordinate is a function of unique phase.

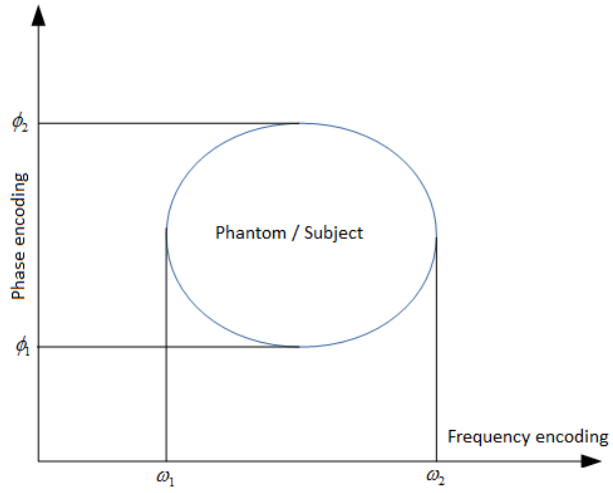

Figure 2.5 (a) Phase encoding in y direction and (b) frequency encoding in x direction

2.1.3 K-Space and image reconstruction

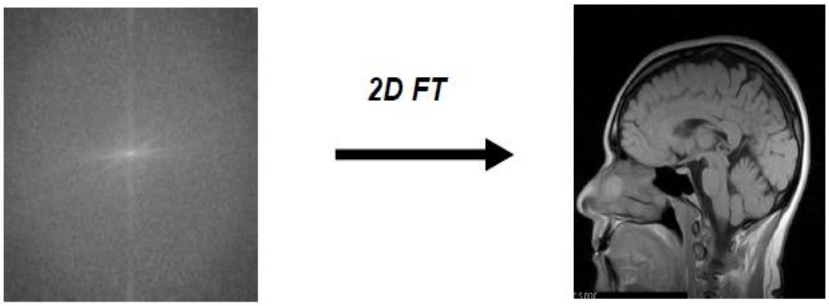

K - space **MR – image**

Figure 2.6 Illustration of reconstruction of an MR image from K – space

In basic terms K-space is a matrix containing the raw data of an MR image. The raw data is a matrix of sampled MR signals and by applying a 2D Fourier transform on this data a final MR image can be reconstructed [14]. The type of Fourier transform is generally a discrete or a fast Fourier transform. A single slice in a particular plane will correspond to a K-space plane

acquired in real-time. Therefore, each point on the K-space includes information related to frequency encoding, phase encoding and signal intensity data. This signal intensity along the x-axis is controlled by frequency encoding gradient while on the y-axis is controlled by the phase encoding gradient. To summarize it can be said that the K-space stores digitized data signals during raw data acquisition, these digitized signals are then sent to an image processor where the Fourier transform is applied to the digitized signals to obtain the final MR image.

2.2 Types of RF resonators

2.2.1 Surface resonators: In practical design of a surface resonator, capacitors in a surface resonator are usually distributed around the circumference of the resonator to improve the current distribution and reduce radiation and electric losses. Despite a high SNR, surface resonators are usually limited in providing a large FOV (field of view), especially in clinical imaging scans. This is because the sensitivity of a surface resonator decreases along with the increment of its size. A typical surface resonator designed and constructed by Ms. Kaci Carter at TBRRI (Thunder bay regional research institute) is shown in Figure 2.7 (a). In order to overcome this problem, one can use multiple small-size surface resonator elements to form a large resonator array, and provide a large FOV without any cost of SNR [7,15] which are termed as phased array resonators.

2.2.2 Birdcage resonators: They possess a cylindrical geometry as shown in Figure 2.7 (b) and are capable of generating a homogeneous magnetic field inside its volume due to their cylindrical shape. They have better B1 field homogeneity as compared to surface and phased array resonators but lack a good SNR. The birdcage resonator requires tuning due to differences in dielectric and conductive loading that will occur when phantoms are placed inside the birdcage resonator [7,14]. The birdcage resonator used in this work is shown in Figure 2.7 (b).

(a) (b)

Figure 2.7: (a) Surface resonators (b) Birdcage resonator

2.3 Basic theory of birdcage resonators

The concept of RF birdcage resonator was introduced by C.E.Hayes *et al*. in 1985 [7]. Since then birdcage resonators have been widely used in MRI because they can generate a homogeneous RF magnetic field in the volume of interest. Birdcage resonators consist of two circular conductive loops referred to as end rings, N conductive straight elements referred to as rungs (or legs) as shown in Figure 2.8 and lumped capacitors on the rungs or end rings or both. According to the location of these capacitors on the resonator geometry, there are three types of birdcage resonators: low-pass, high-pass and band-pass birdcage resonators [8]. They are illustrated in Figure below:

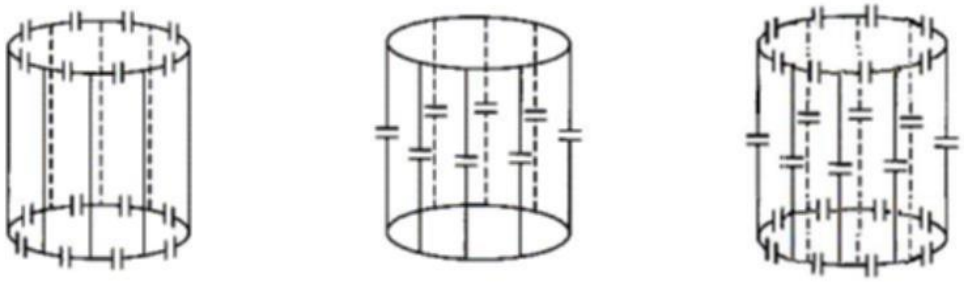

(a) (b) (c)

Figure 2.8: Illustration of birdcage resonator equivalent circuits a) High-pass b) Low-pass c) Band-pass [8]

A birdcage resonator with N number of legs and equal valued capacitors has N/2 distinct resonant modes [8] in which the first mode, is highest frequency resonant mode for high-pass birdcage resonators and is capable to generate a co-sinusoidal current distribution. In order to

generate a homogeneous field in the N-leg birdcage resonator at Larmor frequency, currents in the rungs must be proportional to sinθ (or cosθ), where θ values can be expressed as

$$\theta = \frac{360}{N} i \qquad \text{Where } i = 1, 2 \ldots N \text{ is the rung number in consideration} \qquad (2.7)$$

Producing a co-sinusoidal current distribution in the rungs as well as the desired homogeneous B1 field at the operating frequency is achieved by using the correct capacitance value for the capacitors placed on the end rings. Therefore, finding the necessary capacitance value for the birdcage resonator to resonate at the desired frequency is the starting point of designing a birdcage resonator. Additionally, it is also important to know the complete resonance frequency spectrum of a birdcage resonator that helps the resonator designers to be sure that working mode is far away from the other modes and so that tuning the resonator can be done without interfering with the other modes [8]. Also before the actual construction of the resonator, modeling the resonator in a 3D CAE simulation environment and making EM analysis in the ROI have importance in terms of observing the B1 field distribution inside the birdcage resonator. These B1 field analyses are used to generate simulated B1 field data inside the resonator that can be compared with the experimental data, as done in Chapter 3.

A birdcage resonator is expected to generate a uniform magnetic field inside its volume over ROI. An ideal cosine current distribution on a cylindrical surface generates a homogeneous magnetic field within the birdcage resonator. The current distribution for a birdcage resonator is given by the expression:

$$I_n = I_0 \cos(\pi m n / N) \qquad (2.8)$$

Where I_n the current is in a particular rung, n is the rung number, m is the mode and N is the total number of rungs. m = 1 mode is the preferred mode in MRI for high pass designs [7]. An illustrative current distribution graph for an 8 rung high pass birdcage resonator is shown in Figure 2.9.

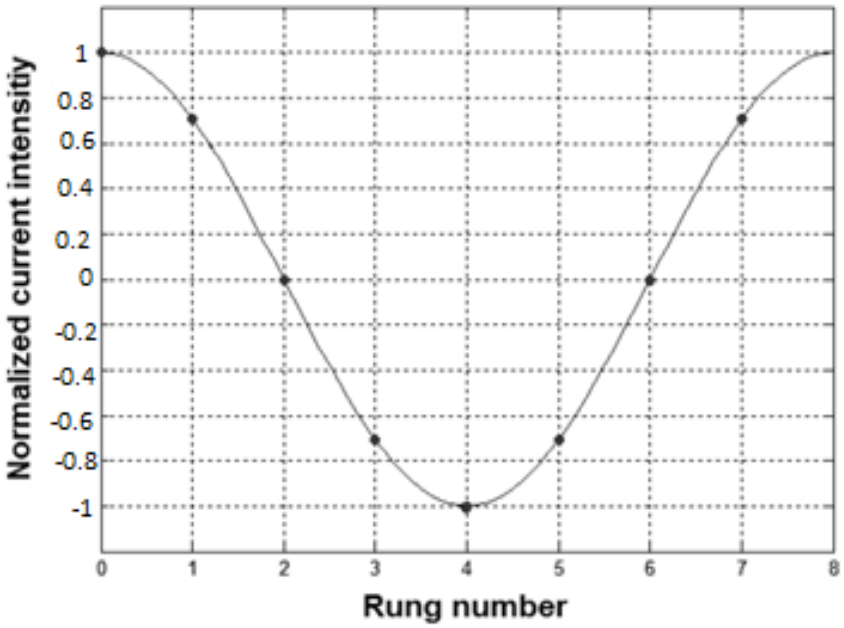

Figure 2.9 Illustrative cosine currents distribution for 8-rungs high pass birdcage resonator [15]

2.4 Analysis of birdcage resonator using lumped elements

A birdcage coil can be considered as a circular network of identical filter elements [15], each of which is connected to another and the last one is connected to the first one to form a circular network. A typical high-pass birdcage resonator and its filter element is shown in Figure 2.10 (a) and its matrix diagram is shown in Figure 2.10 (b).

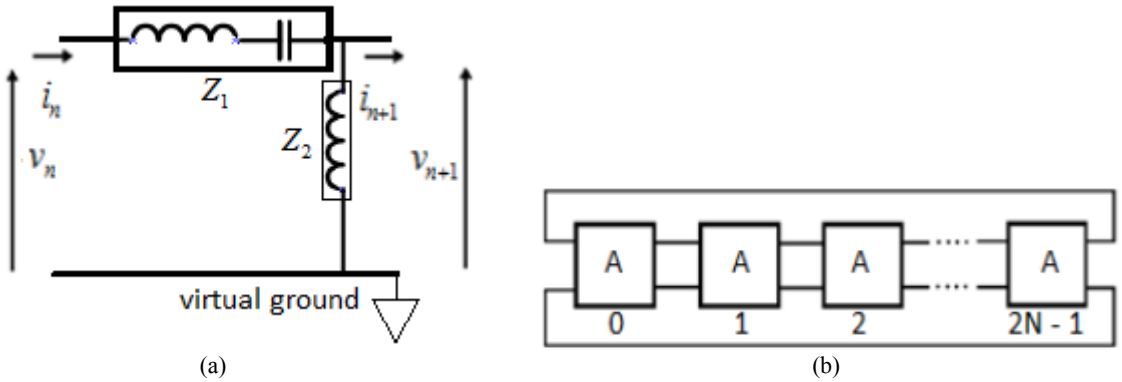

(a) (b)

Figure 2.10 Illustrative schematic of a high-pass birdcage resonator filter element (a), and matrix diagram of a high-pass birdcage resonator (b) [15].

There are many numerical ways to analyze the behavior of a birdcage coil. A method using ABCD matrix is very useful and effective in calculating the resonance mode of a birdcage coil [15]. Considering the filter cell as a network, the total impedance of the end-ring segment consisting of the segment inductance and the capacitance of the end-ring capacitor (since the resonator is a high-pass design) is Z1, and the total impedance of the rung consisting of its inductance (and the capacitance of the rung capacitor if in a low-pass mode) is Z2, respectively, as shown in Figure 2.8 (a). A birdcage resonator of 2N rungs can be then described as a circular ladder network made of 2N elementary networks, shown in Figure 2.8 (b).

Let A be the ABCD matrix of a filter element, described as,

$$A = \begin{bmatrix} 1 + \dfrac{z_1}{z_2} & z_1 \\ \dfrac{1}{z_2} & 1 \end{bmatrix} \tag{2.9}$$

The input and output of this filter element are defined as,

$$\begin{bmatrix} v_n \\ i_n \end{bmatrix} = A \begin{bmatrix} v_{n+1} \\ i_{n+1} \end{bmatrix} \tag{2.10}$$

Note that the input and output of the network are connected together. For a birdcage of 2N identical elements, we apply the ABCD matrix to entire circular network

$$\begin{bmatrix} v_0 \\ i_0 \end{bmatrix} = A^{2N} \begin{bmatrix} v_{2n-1} \\ i_{2n-1} \end{bmatrix} \tag{2.11}$$

Given the fact that the last filter element is connected to the first one, the input ($v_0 i_0$) equals to the output (v_{2n-1}, i_{2n-1}) therefore

$$A^{2N} = I \tag{2.12}$$

Where I represents identity matrix and 2N is total number of rungs. Let [λ] be the diagonal matrix of the eigenvalues of A and U the eigenvector matrix

$$A = U^{-1}[\lambda]U \tag{2.13}$$

Equation (2.12) can then be replaced by

$$[\lambda]^{2N} = I \tag{2.14}$$

Hence the two eigenvalues of A must satisfy

$$\lambda_1^{2N} = \lambda_2^{2N} = 1 \tag{2.15}$$

Therefore the eigenvalues of matrix A can be obtained from,

$$\det(A - [\lambda]) = 0 \tag{2.16}$$

From the above equations, we can obtain the relationship of birdcage resonator resonance modes and the impedances of the end-rings and the rungs is given as [15]:

$$\frac{z_1}{z_2} = -4\sin^2\left(\frac{k\pi}{2N}\right) \tag{2.17}$$

where k is an integer between 0 and N. Equation (2.18) implies that there are k resonant modes in a birdcage coil for the given end-ring segment and rung impedances, which are determined by the coil geometry and tuning capacitors. In this work $k = 1$ mode is considered which is the mode of interest in MRI for achieving a homogeneous B1 field inside the volume of birdcage resonator and value of $N = 4$ should be considered for calculation purposes.

2.5 A high pass resonator design example

This section presents a design example of a 8 rung high pass birdcage resonator where the rung length is 7.3 cm and the length of each section of end ring is 2.5 cm, while the width of the rung and each section of end ring is 0.65 cm. These dimensions are the same to that of the resonator used for this work. The formula for estimating the self-inductance L in μH for the copper strips is

$$L = 0.002l\left(\ln\frac{2l}{w} + \frac{1}{2}\right) \tag{2.18}$$

Where l and w are the length and width (in cm) respectively of the copper strip [8]. For a high pass design from Figure 2.10 and considering the virtual ground,

$$Z_1 = j(\omega L_1 - \frac{1}{\omega C}) \tag{2.19}$$

and

$$Z_2 = j\omega L_2 \tag{2.20}$$

Where L_1 is the self-inductance of each section of end ring and L_2 is half the self-inductance of the rung and C is the capacitance of each end ring capacitor. Using equation (2.18) actual values of L_1 and L_2 are calculated to be 12.8nH and 26.35 nH respectively. From Equation (2.17) let $\frac{Z_1}{Z_2} = a$, to calculate this value it is required to set k = 1, in Equation (2.17). From Equations (2.19) and (2.20) the Equation for C is derived as,

$$C = \frac{1}{\omega^2 (L_1 - aL_2)} \tag{2.21}$$

So by using Equation (2.21) the calculated capacitance of each end ring capacitor is 55 pF. This value is used in Section 2.6 to perform circuit simulations. As advised in [15] the value of effective inductance should be used for a better accuracy instead of self- inductances, the effective inductance values for end ring and the rung were calculated using the Birdcage Builder software equation based calculations are complicated in this case. The Birdcage Builder (www.pennstatehershey.org/web/nmrlab/resources/software/javabirdcage/circular) calculations are shown in Figures 2.11 (a),(b) and (c). The effective inductance values for L_1 and L_2 are calculated to be 16.3nH and 28.03nH respectively.

Using these values in Equation (2.21) the calculated capacitance of each end ring capacitor is 47.4 pF. It should be noted that this is a theoretical example and hence for practical purposes the tuning capacitor value has to be iteratively determined [15] by loading the resonator with a suitable phantom like saline and testing the resonance on a vector network analyzer (VNA). This task of tuning the resonator to the desired Larmor frequency of 127.74 MHz was already performed by Mr. Chris Abraham (at TBRRI) who designed and constructed the resonator used in this work for small animal MRI. For practical purposes the tuning capacitor value was calculated to be 43 pF. The details of capacitance values are presented in Table 2.1.

Table 2.1 : Details of capacitance calculation for 8 rung high pass birdcage

Method used to calculate capacitance value	Capacitance value (pF)
Equation (2.21)	55 pF
Effective inductance from birdcage builder and substituting the same in Equation (2.21)	47.4 pF
Practical tuning with saline phantom	43 pF

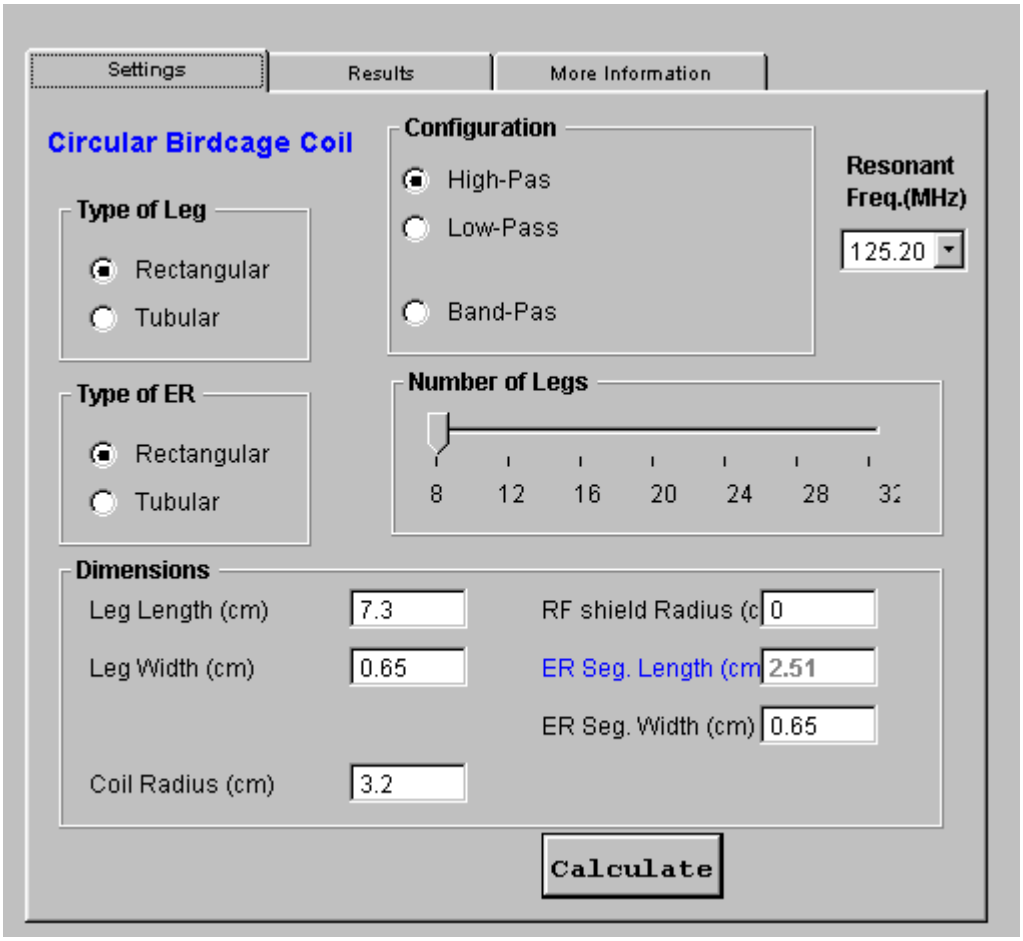

Figure 2.11(a) GUI of the Birdcage Builder [16] (developed by Penn State Center for NMR Research)

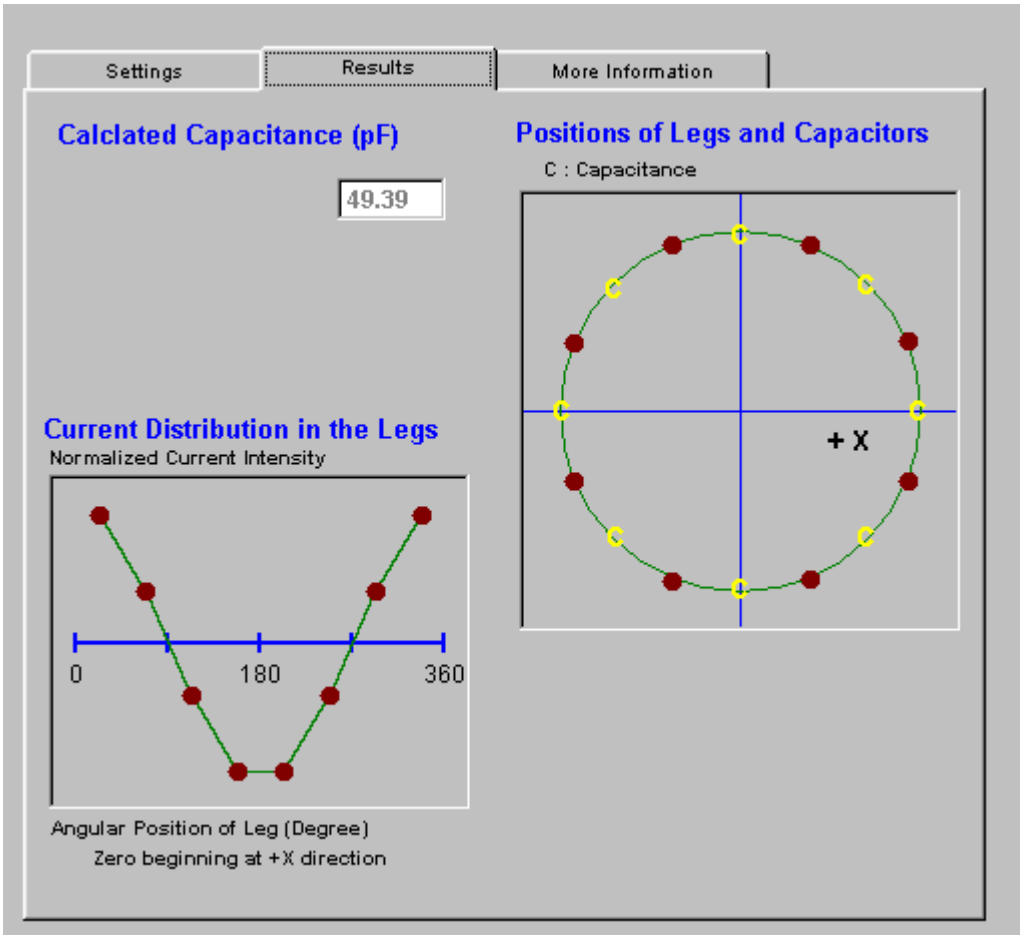

Figure 2.11(b) Capacitance calculation using Birdcage Builder

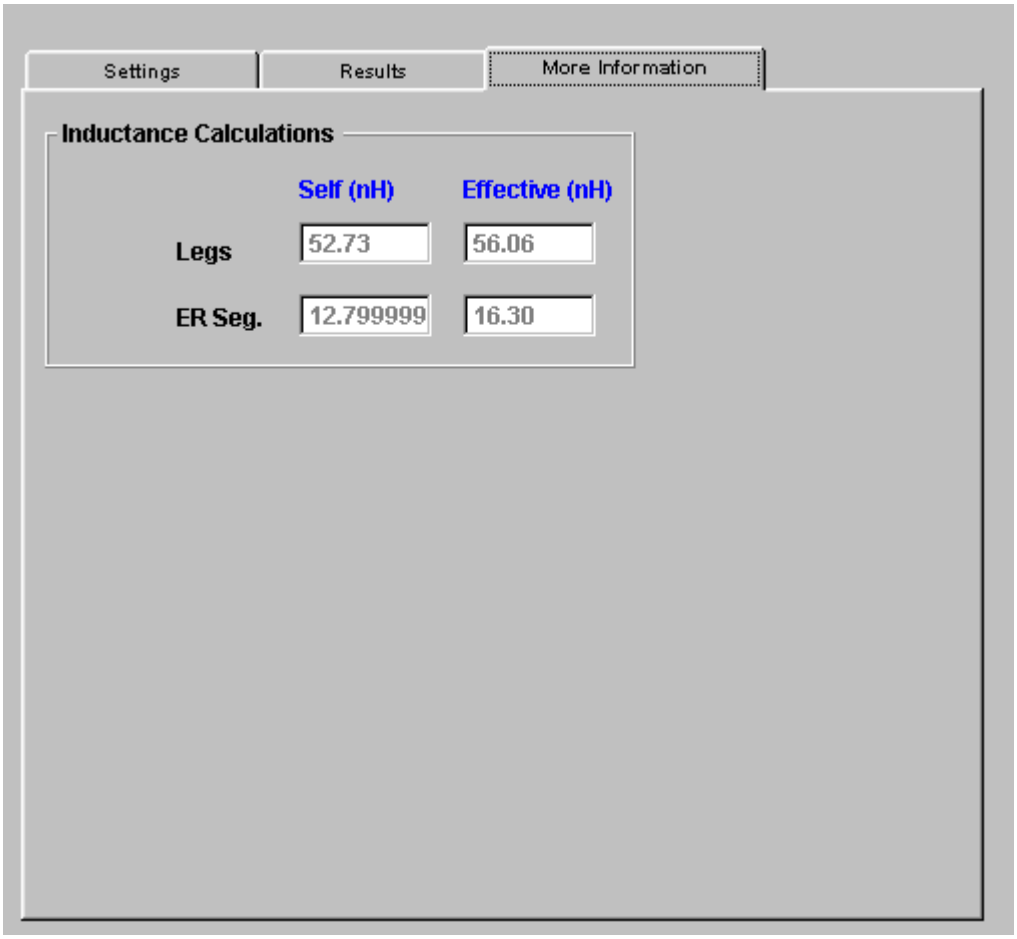

Figure 2.11(c) Inductance calculation using Birdcage Builder

2.6 Circuit simulations

The purpose of this Section is to identify the significant difference in input impedance characteristics for the two different configurations of the input port. Figure 2.12 shows QUCS (Quite Universal Circuit Simulator) designed schematic of the high pass resonator for the port connected between two rungs and its corresponding simulation result is shown in Figure 2.13. A schematic of the resonator with another configuration, where the port is assumed to be connected on one of the rungs [15] is shown in Figure 2.14 and its corresponding result is shown in Figure 2.15. It should be noted that the inductance of the rung is L_3 which is twice that of L_2 as the complete rung is considered in circuit simulations. The resistance of copper strip for each end ring section and rung is approximated using the online resistance calculator

(http://www.eeweb.com/toolbox/trace-resistance) to be 0.00107 ohms and 0.00312 ohms respectively. However the actual resistance on the rung and each section of the resonator may be quite different considering the skin depth and non-uniform current distribution on the surface of copper strips [15].

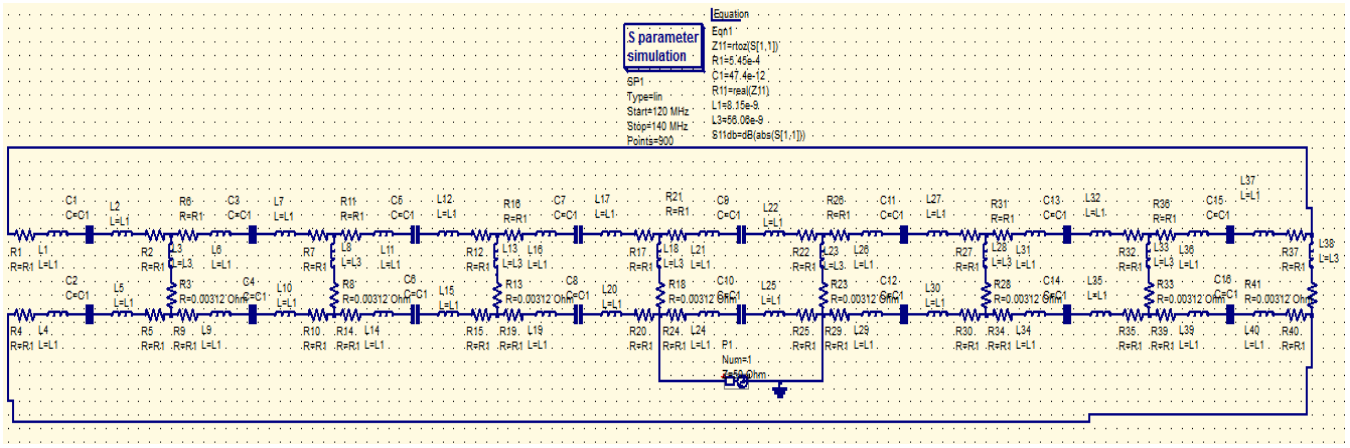

Figure 2.12 Schematic of a high-pass birdcage resonator designed in QUCS for port in between rungs

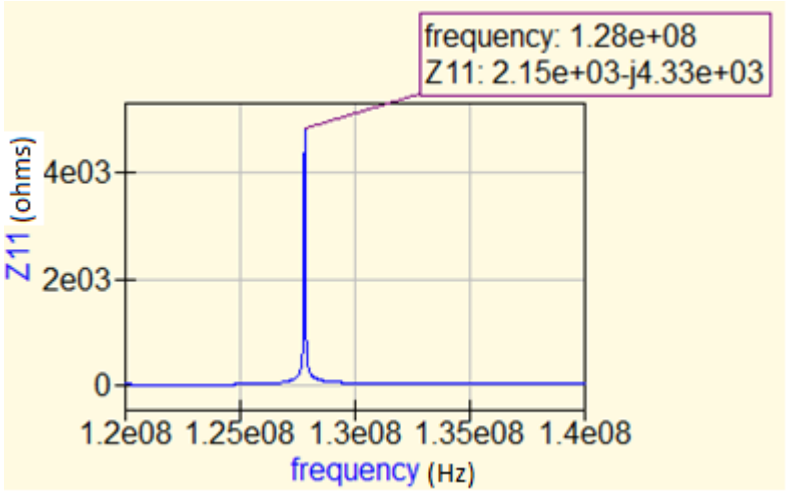

Figure 2.13 Input impedance as a function of frequency for port in between rungs

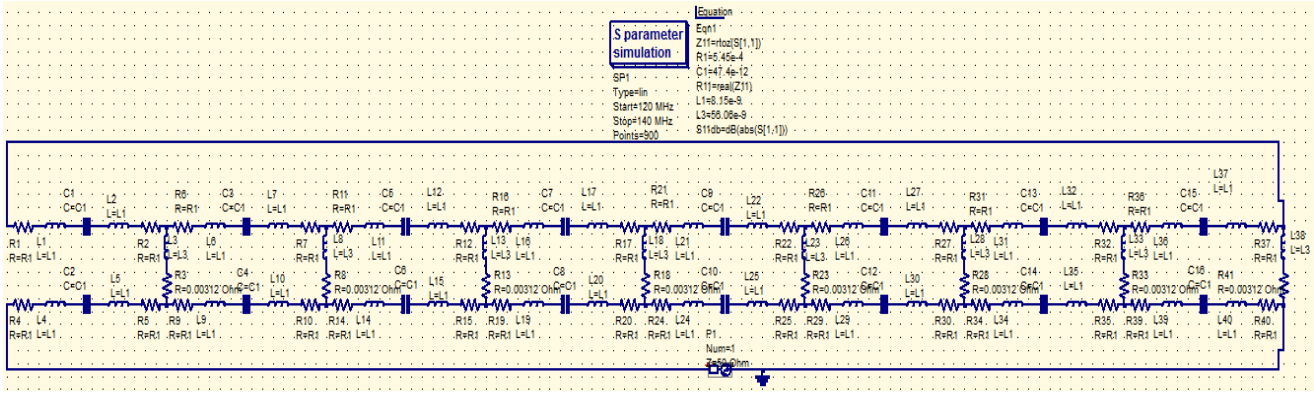

Figure 2.14 Schematic of a high-pass birdcage resonator designed in QUCS for port on a rung

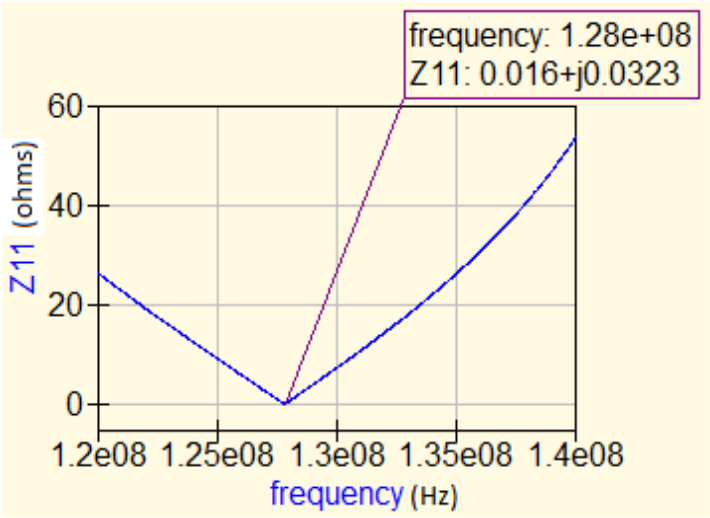

Figure 2.15 Input impedance as a function of frequency for port on rung

2.7 Review of previous studies

Although construction of birdcage resonators are based on the iterative procedures (tuning and matching), there are several techniques proposed in designing and simulating a birdcage resonator in the literature. Note that, we mean computing the necessary capacitance value and modeling the structure of a birdcage resonator in HFSS by saying 'designing a birdcage resonator' and we mean solving for the B1 field distribution inside the birdcage resonator by saying 'simulating a birdcage resonator'. The method for capacitance calculation using [16] has some limitations. First, coupling between opposite end rings is not considered. Therefore, accuracy of the calculated capacitance will decrease when the coil length gets shorter. Second, end ring segments are considered as straight line

segments but in practice this is not the case. Finally, self-inductance and capacitance calculations are made under the quasi-static assumptions. As a consequence of this assumption, error will increase when the desired resonance frequency increases to a point at which the wavelengths are comparable with the resonator dimensions. This assumption is also used in other studies like the low pass and band pass type of birdcage resonators that use lumped circuit element model in order to analyze the birdcage resonator [16]. Even if the quasi-static assumptions seem to have some limitations they are very much valid for this work, because they satisfy an important criteria [17] which is used for determining whether a conducting strip can be modeled as lumped circuit element or not, and is given as

$$\text{Length of conductor} < \frac{\lambda}{20}$$

where λ is the signal wavelength. For more precise tuning of the end ring capacitors and to solve for B1 field distributions inside the resonator volume a full wave 3D EM software can be used. The software package used for this work is HFSS (ANSYS, PA, USA). Using this software package, loaded or unloaded birdcage resonators can be modeled and electromagnetic field calculations inside the resonators can be made [12]. In 1999 J.Jin analyzed B1 field inside birdcage resonator using FEM [8]. Recently Collins *et al* [18] has shown B1 field mapping for human phantoms using 3D EM modeling. Some other studies using full birdcage resonators are [19,20] while those relating to half birdcage resonators are [21,22,23]. It is expected that the half birdcage resonator described in Chapter 4 exhibits a co-sinusoidal current distribution similar to the full birdcage which in turn produces a homogeneous B1 field inside its volume [21]. Literature is also available on B1 mapping for MRI scanners (embedded code) [24] which is employed in this work to deal with big peaks in B1 maps caused due to susceptibility issues [24], discontinuities introduced by solder imperfections that further complicate the comparison between HFSS and MRI generated B1 maps. The method employed to deal with these issues is presented in Section 3.4.

2.8 Practical considerations

Practical considerations include typical input power fed to the resonator and peak voltages in capacitors. The input power applied to the resonator in this work was 70 W. Typical input

power values for birdcage resonators could range anywhere between 50 to 350 W for small animal imaging experiments depending upon the capacitor values and geometric dimensions of the resonator in order to generate a sufficient B1 field for obtaining an high contrast image. The peak voltage for a capacitor on the 8 rung high pass resonator is approximately estimated to be around 235 V [15]. This value obtained from QUCS is 221 V as shown in Figure 2.16. In practice while ordering the capacitors for constructing the birdcage resonators high voltage values are considered usually up to 500 V so that they are capable to withstand equivalent RF power inputs. Although the peak voltage value may not be exactly the same in all the capacitors but will be more or less uniform due to the resonance phenomenon.

acfrequency	Pr1.v
1.28e08	221 / -10.3°

Figure 2.16 Peak voltage across capacitor obtained from QUCS for circuit shown in Figure 2.12

In order to assure maximum power dissipation to the load and minimize the reflection, the impedance of the load should be maintained the same as that of the transmission line (generally 50 Ω). Another important and allied practical consideration is the RF heating of the resonator. It is observed during experimentation that the resonator used in this work is able to withstand the input power of 70 W, as no acrylic melting was seen on the resonator surface while performing MRI experiments which suggests that conductor heating is not an issue for the resonator. In general $60\,^{o}C$ is considered as the maximum operating temperature inside the complete volume of the resonator around the rings and rungs in small animal MRI since they are the only conductive parts of the resonator. Although RF heating is not the main objective of this work but a temperature profile of the resonator was plotted in HFSS and its result is presented in Appendix A.2. The input impedance of a birdcage resonator is a function of the dimensions of the copper strips and the overall impedance of the resonator (which is a function of the overall construction of resonator including the capacitance values). The length and width of the copper strips can be optimized using HFSS in order to match the input impedance of the resonator to 50 ohms, in case a specific resonator design is not available. Another technique

that may be used to optimize the input impedance of resonator to 50 ohms when exact specifications of the resonator are not available is, Space-Mapping Optimization With Adaptive Surrogate Model [25]. One of the limitations of this technique is that, it may not be possible to define the surrogate model with losses. To use this technique it is necessary to at least have an approximate model of the resonator along with the equivalent circuit model of the resonator. After this the length, width and thickness of the copper strips can be iterated using this technique to optimize the input impedance of resonator to 50 ohms. The conductivity values of the phantom materials also play an important role in determining the input impedance of loaded birdcage resonators at a particular frequency of operation.

It might be useful in some practical situations to compare the B1 field distributions of the half birdcage resonator to that of the full birdcage resonator. This will be a useful comparison where full birdcage geometries have a positional constraint, For example, MR guided HIFU (High intensity focused ultrasound) where the transducer is placed underneath the HIFU platform or MRI of adult human shoulder. It should be noted that the theory mentioned in [21] allows the possibility of positioning two half birdcage resonators in such a way that resulting B1 field distribution is identical to that of a full birdcage resonator of the same size. This suggests that a full birdcage resonator can be bisected into two half birdcage resonators provided the axis of cylindrical symmetry is correctly determined.

2.9 The finite element method (FEM)

FEM is a numerical method for obtaining solutions to practical problems of engineering electromagnetics. It was first proposed in 1940s by Courant [26] to solve problems in vibration engineering. Thereafter this method was developed and applied extensively to problems of elasticity, structural engineering, computational fluid dynamics and computational electromagnetics. The first paper on the application of FEM to EM problems appeared in 1968 by S.Ahmed [27] and since then FEM has been widely employed by workers to seek solutions for EM fields of advanced electrical engineering devices like antennas, micro strips, microwave devices, RF resonators etc. FEM is one of the most widely used method to solve for EM fields inside volumetric structures. The process of extracting EM fields from any

structure using FEM is the most critical one. FEM predicts EM fields by discretizing the entire structure with the help of various standard geometric shapes like triangles, squares, rectangles in 2D and tetrahedrons and cubes in 3D, out of which the triangles and tetrahedrons are most commonly employed because they conform to complex geometries easily [28], as shown below. The collection of these triangles and tetrahedrons is called the 'FEM mesh' and it is illustrated in Figure 2.17.

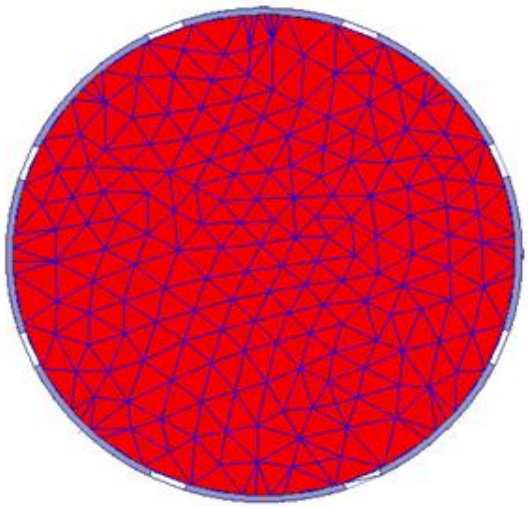

Figure 2.17: Illustration of an initial triangular mesh in cross section of 8 rung high pass birdcage resonator generated in HFSS

2.9.1 Notations for fields and phasors

The MKS system of units is used throughout this thesis. The script quantities represent time-varying vector fields and are real functions of spatial coordinates *x, y, z*, and the time variable *t*. These quantities are defined as follows:

$\bar{E}$ is the electric field, in volts per meter (V/m).

$\bar{H}$ is the magnetic field, in amperes per meter (A/m).

$\bar{J}$ is the electric current density, in amperes per meter squared (A / m^2).

$\bar{B}$ is the magnetic flux density, in Tesla (T).

As recommended by the IEEE Standard Definitions of Terms for Radio Wave Propagation, IEEE Standard 211-1997, the terms electric field and magnetic field are used in place of the older terminology of electric field intensity and magnetic field intensity.

2.9.2 Theory of FEM method

FEM solves for electric fields using the Helmholtz equation, which is given as

$$\nabla \times (\frac{1}{j\omega\mu} \nabla \times \bar{E}\ ) + j\omega\varepsilon\bar{E} = -\bar{J} \tag{2.22}$$

Where ω is the frequency at which EM field solution is obtained in rad/s, μ is the permeability of the material in H/m and ε is the permittivity of the material in F/m. Equation (2.22) can be derived from Maxwell's equation which is,

$$\nabla \times \bar{E} = -j\omega\bar{B} \tag{2.23}$$

FEM then calculates the magnetic field $\bar{H}$ using the equation

$$\bar{H} = \frac{j}{\mu\omega} \nabla \times \bar{E} \tag{2.24}$$

Multiplying both sides of Equation (2.22) by a basis function $\bar{W}_i$,

$$\bar{W}_i.((\nabla \times \frac{1}{j\omega\mu} (\nabla \times \bar{E})) + j\omega\varepsilon\bar{E}) = \bar{W}_i.(-\bar{J}\ ) \tag{2.25}$$

The basis function inside a tetrahedron (finite element for 3D case) can be defined on each edge in [29].

After applying the basis function, the FEM weak form (The form obtained by integrating any FEM equation is called its weak form [29]) is,

$$\int_v \bar{W}_i.((\nabla \times \frac{1}{j\omega\mu} (\nabla \times \bar{E})) + j\omega\varepsilon\bar{E})\, dV = \int_v \bar{W}_i.(-\bar{J}\ )\, dV \tag{2.26}$$

then using the curl of curl identity,

$$\int_v ((\frac{1}{j\omega\mu} (\nabla \times \bar{W}_i).(\nabla \times \bar{E}) - j\omega\varepsilon\bar{E}.\bar{W}_i)\, dV = \int_v \bar{W}_i.(-\bar{J}\ )\, dV \tag{2.27}$$

the electric field for a given finite element (for example, a tetrahedron) is expanded using basis functions and is given by,

$$\bar{E} = \sum_i (E_i . \bar{W}_i) \tag{2.28}$$

Where, E_i are unknown coefficients.

Equation (2.28) is substituted into Equation (2.27) and the resulting equation is solved analytically. The result is a linear system of equations for each tetrahedron. The matrix for this linear system is called a local matrix. Now to account for all the tetrahedrons a global matrix is required [26] which contains the contribution of all the local matrices. FEM solves this global linear system to find the unknown E_i coefficients for all tetrahedrons.

2.9.3 Merits of FEM

1. It is one of the suitable numerical methods to solve Maxwell's equations [30,31] which form the basis of electromagnetics because FEM is specifically suitable to seek solutions of partial differential equations (PDE's) and Maxwell's equations are a set of PDE's.

2. It has the capability to calculate near EM fields inside closed structures [30,31].

3. It has the capability to handle extremely fine mesh including any unstructured mesh, meaning that the variation in the input power to any electrical device can be more finely represented [30,31] and therefore the field calculation by spatial differentiation of the particular input power can be more accurately performed.

4. It can solve simultaneously for EM fields, resonance modes and current distributions [30,31].

5. FEM simulations solve 3D full wave Maxwell's equations and hence there is very little room for any assumptions except the fact that the radiation boundary walls need to be truncated which is one of the boundary condition that assumes that EM waves vanish after traveling a certain distance [30,31].

6. FEM possess minimum discretization error as compared to other methods like finite difference method (FDM), which is also a numerical method used to compute EM fields [28] and the FEM triangular elements conform well to curved surfaces. This is shown in Figure 2.18.

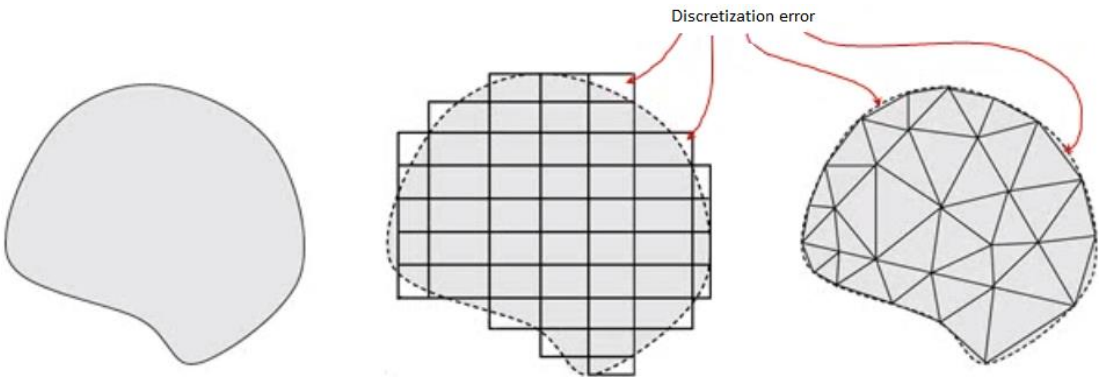

(a) Arbitrary object **(b) FDM mesh** **(c) FEM mesh**

Figure 2.18: Comparison of FDM and FEM mesh

2.9.4 Limitations of FEM

1. Highly complex implementation specifically for non-symmetric 3D structures. This is because symmetric structures can be modeled with 2D approximations and their EM field results can be applied in 3D space, but this is not the case for non-symmetric 3D structures as 2D approximations are no longer valid.

2. Steep learning curve as compared to RF circuit simulators because user very often needs to heal structures to make them eligible for 3D full wave EM simulations while using commercial FEM solvers like HFSS [28]. Healing is the process in CAE modeling that repairs overlapping surfaces and volumes by introducing an infinitesimal gap in between them [28].

3. Very fine concentration of elements is required in areas where the potentials, currents vary and hence the EM fields change abruptly. Mapping of such EM fields require above average computing resources which are expensive [30,31].

4. Overlapping of surfaces and volumes is not permitted, which is not the case in practical scenarios. This is one of the reasons the structures need to be healed.

Chapter 3
EM simulation and validation of birdcage resonator

3.1 Introduction

This chapter deals with full wave EM simulations of the birdcage resonator performed in HFSS. In Section 3.2 of this chapter, these models are explained with respect to finite element modeling: geometry, material properties assignment, excitations and boundary conditions which are major requirements to set up the resonator model in HFSS, commonly known as computer aided engineering (CAE) analysis. Next, the EM frequency domain analyses that were undertaken using the FEM models of high-pass birdcage resonators developed in HFSS are discussed in subsequent sections; these sections provide the details about the three different case studies performed in this work. Further the EM simulations were compared with the MRI scans performed at TBRRI on a Philips Achieva 3T MRI scanner.

The 8 rung birdcage resonator was built by using copper tapes sticking to the surface of a machined acrylic tube. Dimensions of the coil were carefully designed for an optimized filling factor and its suitability for small animal MRI experiments. The dimensions of the resonator are as mentioned in Table 3.1. Eight gaps were made on each end-ring to accommodate all 16 capacitors, to design a high-pass structure.

3.2 Design of high pass birdcage resonator in 3D CAE environment

In this section, high-pass birdcage resonator (structure) developed in HFSS is discussed, as shown in Figure 3.1, while Figure 3.2 shows the photograph of the birdcage resonator used for MRI. We first start with the geometry of the structure. The procedure of modeling the high pass birdcage resonator in HFSS is analogous to the procedure followed to practically build the high pass birdcage resonator. The starting point was the grid set up in HFSS workspace, and next was the design of two concentric cylinders of required resonator dimensions in HFSS which will form the acrylic plastic former. After that, it was required to break either the top or bottom surface of these cylinders into N equal arcs, where N is the number of rungs of the high pass birdcage resonator. It should be noted that the numbers mentioned in Figure 3.5 are the

rung numbers. The geometric details of the resonator are presented in Table 3.1. Eight gaps were made on each end-ring to accommodate all 16 capacitors, forming a high-pass structure. Then the end rings were constructed in such a way so as to accommodate the equal valued capacitors on the top and bottom end rings of the resonator as shown in Figure 3.1. In this work N = 8, meaning this work deals with a high pass birdcage resonator with 8 rungs.

Table 3.1: Geometric details of 8 – rung high pass birdcage resonator

Diameter (mm)	Resonator length (mm)	Rung length (mm)	Rung width (mm)	End ring width (mm)	Thickness of rung and ring (mm)	Thickness of frame (mm)	Tuning capacitors (pF)
64	95	73	6.5	6.5	0.06	3	43

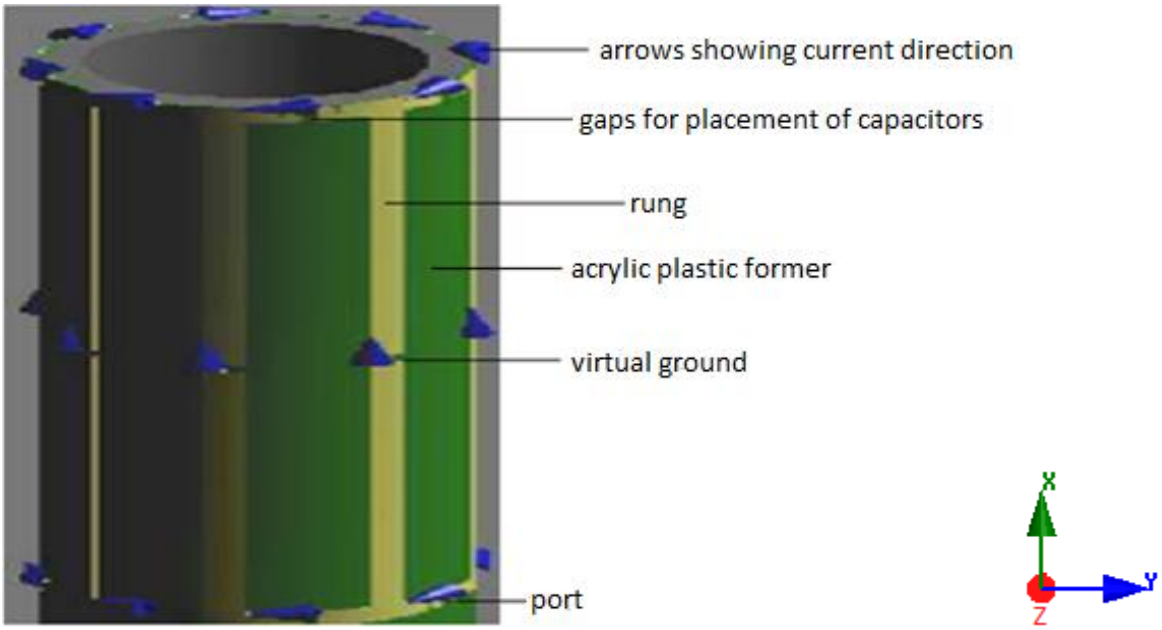

Figure 3.1: Illustrative structure of 8 rung MRI birdcage resonator

Figure 3.2: The 8 rung high pass birdcage resonator used for MRI (also showing a construction defect)

3.3 Simulation set up of high pass birdcage resonator in 3D CAE environment

Inductance, capacitance and electric conductor (copper) boundary conditions were added to the resonator model in HFSS to facilitate the inclusion of their effects in the simulation results. A radiation boundary (box) condition is also added to the HFSS simulation. An RF power of 70 W was fed to the resonator in order to perform an MRI scan; hence, the same was maintained in HFSS simulations as the input power value. The reference B1 was normalized to a value of 1 for experiments and simulations. To specify where on the surface of the resonator inductance and capacitance boundary conditions should be added, the current and voltage had to be controlled and a definition of the current flow line was necessary [30]. In HFSS the selection field for the current flow line initially appeared as undefined, so the user must manually draw the current flow line on the capacitance boundary surface. After this the material properties were assigned to the resonator parts and the details of the same are presented in Table 3.2. It should be noted that B1 fields were mapped only inside a 5mm thick slice at the center of resonator in order to maintain similarity with experiments and conserve computing resources.

Table 3.2: Material details of the 8 – rung high pass birdcage resonator

Part	Material	Relative permittivity	Relative permeability	Conductivity (S/m)
Resonator frame	Acrylic tube	3.4	1	0
Rings & Rungs	Copper tape	1	1	5.8e7

The next step in setting up the simulation was to define the excitations. Excitations are sources of EM fields in any RF device. In this work there was only a single port excitation associated with the resonator, which meant the resonator was linearly excited. In this work the lumped port excitation in HFSS was used to excite the resonator linearly. Lumped ports support single mode excitations especially when S-parameters have to be extracted for any RF device from HFSS. It should be noted that the single port excitation for all HFSS simulations mentioned in this thesis were connected to rung number zero as shown in Figures 3.5, 3.10 and 3.15 meaning the first rung, as mentioned in [15] to generate a homogeneous B1 field. This corresponds to Figure 2.14 for circuit simulations. But this is different in the physical resonator, where the port is connected in between two rungs. Thus the simulated input impedance is not expected to agree with the measurements, but the resonance frequency should be the same as it was shown in Section 2.6. After this step, the solution set up was defined in HFSS. This was the step where the Larmor frequency was introduced to the simulation. The Larmor frequency in consideration was 127.74 MHz, which is the frequency at which B1 field distribution was being queried inside the volume of birdcage resonator. Further, a frequency sweep was defined in HFSS to validate the resonance of the birdcage resonator. The next step was solving the resonator design to seek EM field solutions using FEM. The time required to solve any structure to seek EM field solutions using HFSS depends on geometric complexity, the solution frequency (in this work the Larmor frequency) and available computing resources. The simulations were performed on a computer with Intel core i3 processor with 8GB RAM and a 64 bit operating system. In general, the complete simulation methodology employed by HFSS is depicted in Figure 3.3.

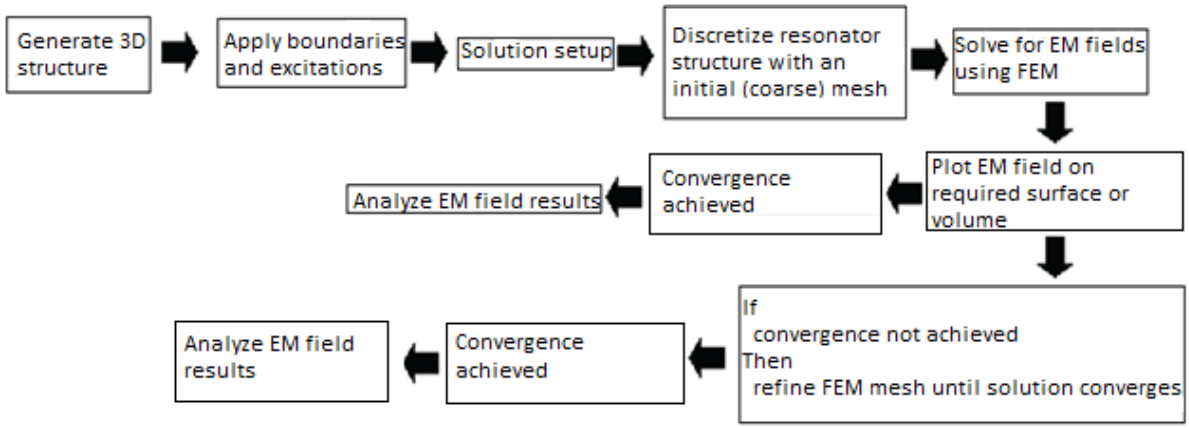

Figure 3.3: Simulation methodology implemented by Ansys – HFSS

3.4 Calculation of scaling factor

MRI employs image processing [1] that scales the measured B1 field values using an unknown factor; hence, there arises a need to estimate this factor to make the measured and simulated B1 field values comparable. The scaling factor was estimated by selecting a 5 X 5 pixel square at the center of the B1 maps from MRI and HFSS and calculating the average of all values in each square . The ratio between these two averages was used as an estimation of the scaling factor.

3.5 Mineral oil phantom

3.5.1 Methods for MRI acquisition and MR image processing

In this first case study the MRI B1 map was acquired using a mineral oil phantom. The reason to use mineral oil phantom is that mineral oil has a short T1 which helped to provide quick, detailed and high contrast MR images. T1 is defined as the measure of the time taken for spinning nuclei to re-align with the equilibrium state or longitudinal axis [14]; it is also called longitudinal relaxation time. Another reason to use mineral oil is that it has dielectric properties similar to fat [14]. Hence the use of mineral oil is a test of resonator similar to a real life scenario. For MRI the mineral oil phantom (452213195310, 3.0T, Philips Healthcare Netherlands) was used, whose details are mentioned in Table 3.3 and the phantom is as shown in Figure 3.4. The HFSS model set up is shown in Figure 3.5. During MRI the mineral oil

phantom was placed inside the resonator as shown in Figure 3.5 to simulate a small animal MRI scan. It should be noted that there was an air gap left in between the mineral oil phantom and the birdcage resonator as shown in Figure 3.5. The maximum air gap in this case was 4 mm. The method used to generate B1 field maps from MRI is called the Dual Angle Method (DAM). With this method, two RF pulses were automatically applied to excite the magnetization to the required two flip angles [34]. After the MRI was performed, the raw data of images were imported and processed in MATLAB (The Mathworks, Natick, USA), using its inbuilt dicom function. The method used here was B1 mapping with embedded code [24] along with the technique presented in Section 3.4.

Figure 3.4 :Photograph of mineral oil phantom

3.5.2 Methods for HFSS simulation and HFSS data processing

A cylindrical shaped phantom with properties of mineral oil as mentioned in Table 3.3 was designed in HFSS and then loaded inside the resonator to mimic the experimental set up as shown in Figure 3.5. The simulation set up was linearly excited with a 70 W input power to seek B1 field distribution inside the volume of the resonator. Once the B1 field distribution inside the volume of the resonator was obtained, data were copied to a stack inside the HFSS

fields calculator, exported to MATLAB and further processed to extract B1 field maps as shown in Figure 3.6.(b). A similar type of normalization as mentioned in Section 3.5.1 was used to process B1 field maps from HFSS to facilitate their comparison with the MRI B1 field maps.

3.5.3 Methods for resonance measurement

The resonant frequency was measured using an Agilent technologies E-507IC VNA (Vector Network Analyzer) available at communications laboratory (room 4002 ATAC building in Lakehead University). Before beginning the measurements, the VNA was calibrated using the open, closed and 50 ohm loads. To measure the resonance at the frequency, the S-parameter option (S11) from the format tab of VNA was selected. The center frequency of the VNA was set to 128 MHz with a 8 MHz span. A similar type of S-parameter extraction was done from HFSS simulations by setting up a frequency sweep from 124 MHz to 132 MHz while the center frequency was kept the same as solution frequency i.e. 127.74 MHz. The S-parameters obtained from experiment and HFSS were exported and saved to touchstone format (s1p files) and plotted in QUCS, the results of which are shown in Figure 3.7 (a). The input impedance results from experiment and simulation are shown in Figure 3.7 (b).

Table 3.3:- Details of the mineral oil phantom used for MRI and Simulation

Shape	Dimensions (mm)	Material	Relative permittivity	Relative permeability	Conductivity (S/m)	Temperature in degree Celsius
Cylindrical	Length = 95 Diameter = 60	Mineral Oil	2.7	1	0	20

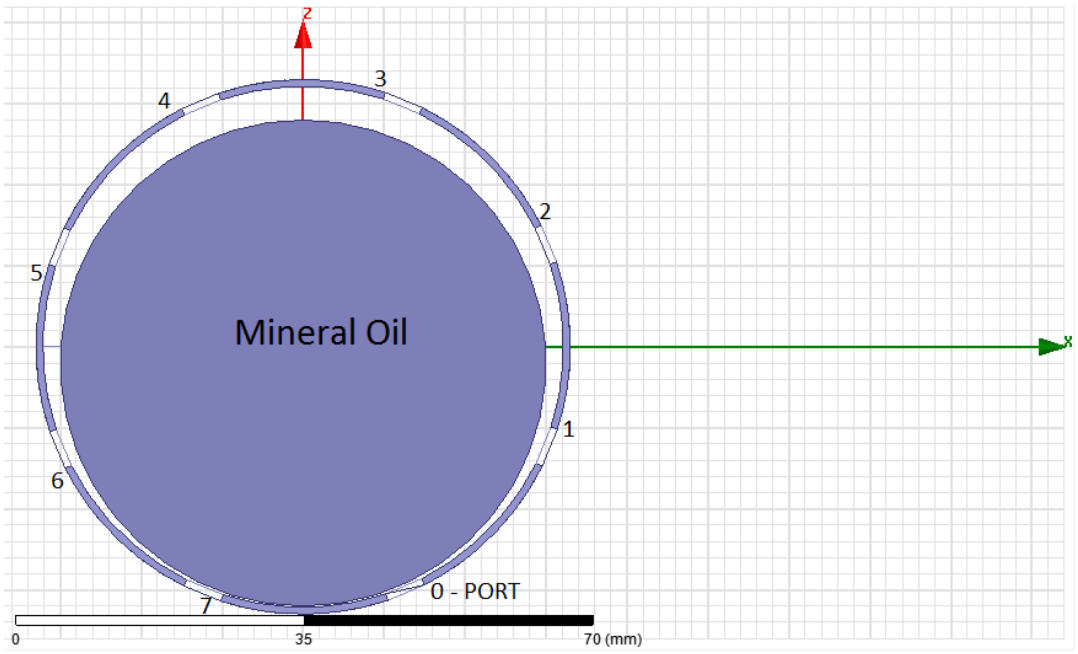

Figure 3.5: Illustration of placement of mineral oil phantom inside birdcage resonator in HFSS

The sequence parameters used to obtain the B1 field map are presented in Table 3.4. Terminologies used in Table 3.4 are as defined below:

FOV (Field of View) is defined as the size of the two or three dimensional spatial encoding area of the MR image. Units: mm^2.

TR (Repetition time) is defined as the amount of time that exists between successive pulse sequences applied to the same slice. Units: milliseconds.

TE (Echo time) represents the time in between the application of the RF pulse and the peak of the echo signal. Units: milliseconds.

Table 3.4:- Sequence parameters used to obtain B1 field maps

Sequence	Method	View	FOV(mm^2)	TR/TE(ms)	Resolution	Slice thickness(mm)
2D FFE	Dual angle post processing embedded in Philips 3T Achieva	Transverse	350*350	1036.27/3.41	128*128	5

3.5.4 Results

Normalized B1 field maps obtained from MRI and HFSS are presented in Figure 3.6 while graphical representation of B1 field data is shown in Figure 3.6. It is observed from Figures 3.6.(a) and 3.6.(b) that B1 field behaviors from MRI and HFSS are similar. The probable reasons for the variations are mentioned in Section 3.5.5. Graphical representation of B1 field data in Figure 3.7 (a) represents normalized B1 field values on the vertical axis almost passing through the center of the phantom while Figure 3.7 (b) represents normalized B1 field values on the horizontal axis almost passing through the center of the phantom. These axes were chosen to plot B1 field data in order to evaluate the same in the center region of the coil, where the small animal is generally placed for an MRI. Figure 3.8 (a) shows that the loaded resonator constructed for MRI and designed in HFSS resonates around the desired Larmor frequency of 127.74 MHz which can be compared, but the input impedance values are not expected to be the same as per reasons mentioned in Section 3.3. It should be noted that S22 was just the name given to the port in QUCS for experimental data, there is only single port excitation associated with the resonator and the name S22 should not be related to S-parameters of any other port. A circular region with 40 mm diameter was chosen at the center of the resonator for quantitative inhomogeneity study. The average normalized B1 from MRI and HFSS throughout this region was computed to be 0.5299 with a standard deviation of 0.077. Therefore the variation of the B1 field strength in this region of resonator is about 14%.

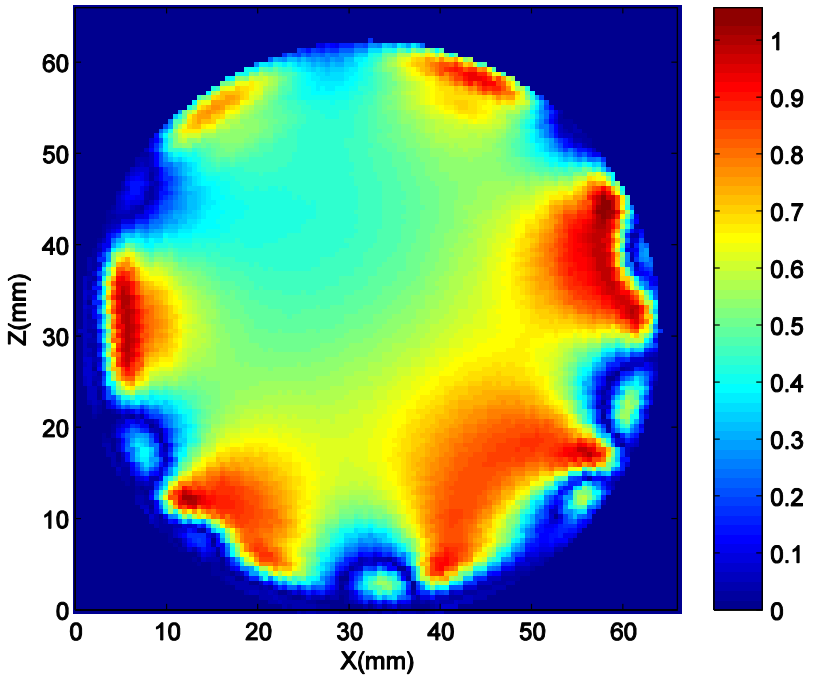

(a)

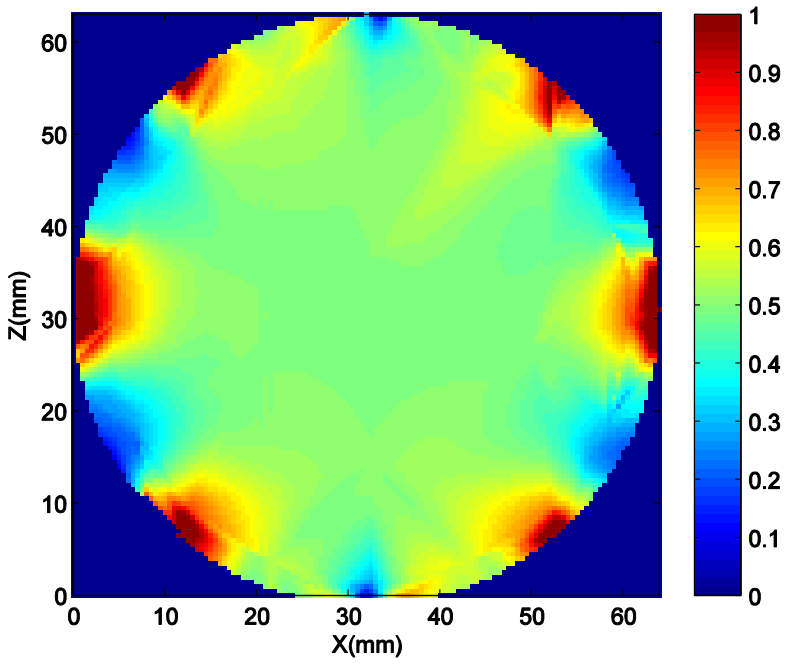

(b)

Figure 3.6: (a) Normalized B1 map generated from MRI (b) Normalized B1 map generated from HFSS simulation

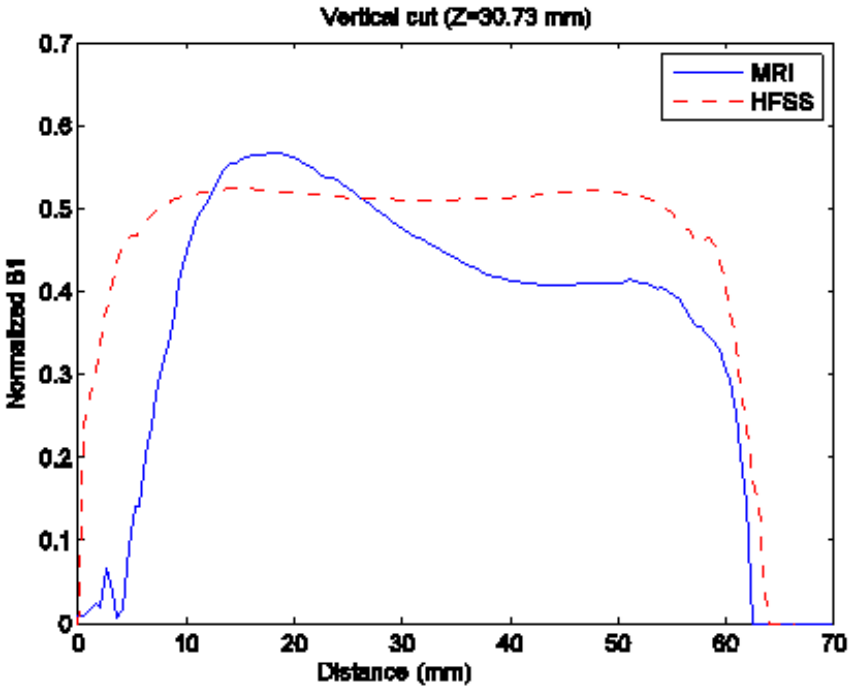

(a)

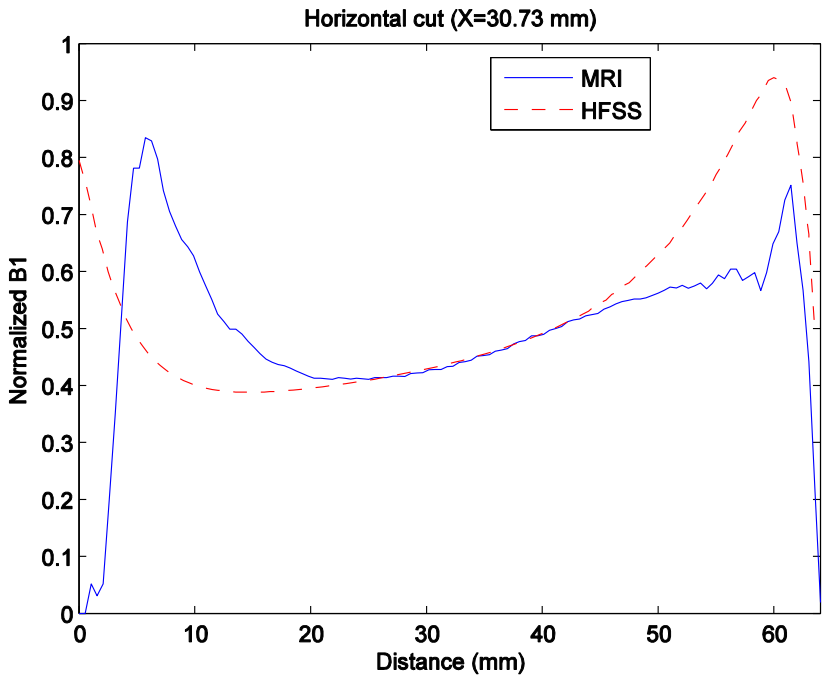

(b)

Figure 3.7: Graphical representation of B1 field data for mineral oil phantom, vertical cut(a) and horizontal cut(b)

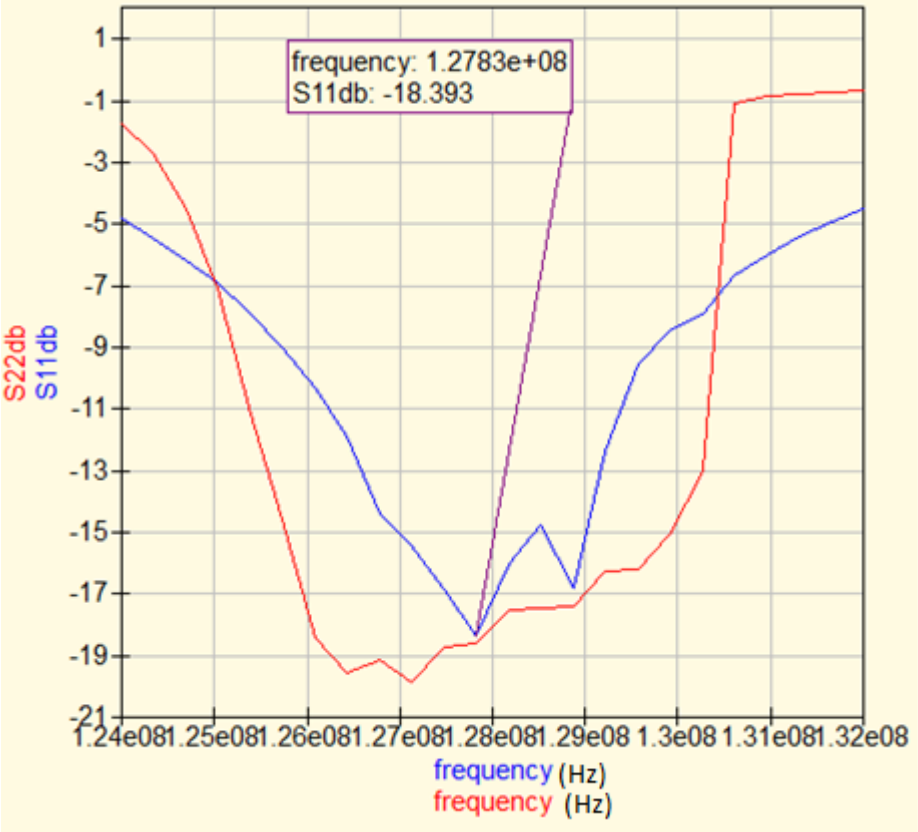

Figure 3.8 (a): S11 response with mineral oil phantom, simulated (blue) and experimental (red)

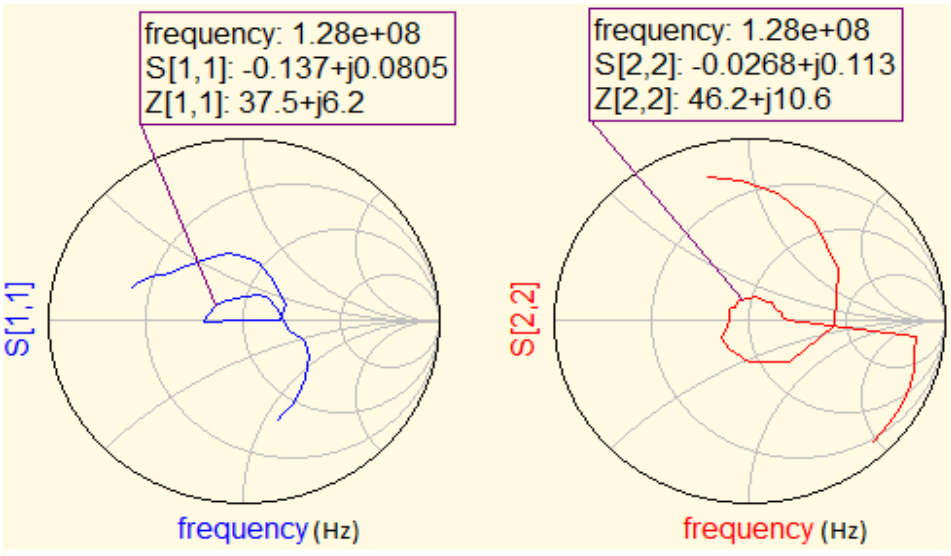

Figure 3.8 (b): Smith chart showing input impedance with mineral oil phantom, simulated (blue) and experimental (red)

3.5.5 Discussion

Figures 3.6 (a) and (b) show that HFSS generated B1 maps have a better homogeneity than the ones generated by MRI. Poor homogeneity and difference in MRI B1 maps in comparison to HFSS B1 maps can be attributed to construction defects such as rungs not being exactly parallel to each other and one of the rungs soldered in the middle as shown in Figure 3.2. Other factors for B1 field variation often seen in magnetic resonance images can be caused by in-homogeneous RF excitation [32], non-uniform reception coil sensitivity, eddy currents driven by field gradients [32] and the electrodynamic interactions with the phantom often described as RF penetration and standing-wave effects [32]. While this is not the case with HFSS wherein the RF excitation was homogeneous while reception of RF signal could not be modeled. B1 field data from Figure 3.7 on the vertical and horizontal axis suggested that B1 field generated by the resonator is mostly homogeneous at the center but varies towards the periphery of the resonator because of the presence of rungs. Figure 3.6 (a) suggests that on the vertical axis the normalized B1 field starts with a higher value at the bottom and decreases with an increase in distance at center as shown in Figure 3.7 (a). The simulation time for this case in HFSS was approximately 5 hours and 30 minutes.

3.6 Saline phantom

3.6.1 Methods for MRI acquisition and MR image processing

A handmade saline phantom was used for MRI (shown in Figure 3.9 and detailed in Table 3.5). In this case the diameter of the cylindrical bottle is almost equal to that of the resonator and hence the saline phantom fits the resonator better than the mineral oil phantom. The saline phantom was used to understand the B1 field behavior in practical MRI scenarios, as salt and water are major components of human tissues [33]. Another purpose was to compare the B1 field distribution inside saline with that of mineral oil. In this case the phantom completely occupied the resonator volume and the port was located on the positive end of the X-axis as shown in Figure 3.10. A cylindrical shaped phantom with material properties of saline was designed in HFSS and loaded inside the resonator in order to mimic the experimental set up as shown in Figure 3.10. The geometric and material properties of glass were not added to the phantom. Apart from these the other methods relating to HFSS simulations and resonance measurement are almost the same as mentioned in Section 3.5.

Table 3.5:- Details of the saline phantom used for MRI and Simulation

Shape	Dimensions (mm)	Material	Relative permittivity	Relative Permeability	Conductivity (S/m)	Temperature in degree Celsius
Cylindrical Bottle	Length = 95 Diameter = 64	150 millimolar saline inside glass bottle	81	1	4	20

Figure 3.9 : Saline phantom used for MRI

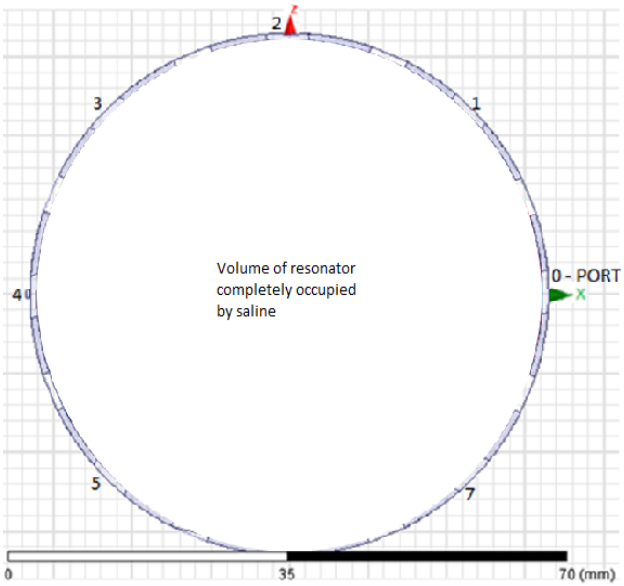

Figure 3.10 Illustration of resonator model loaded with saline phantom designed in HFSS

3.6.2 Results

Normalized B1 field maps obtained from MRI and HFSS are presented in Figure 3.11 while graphical representation of B1 field data is shown in Figure 3.12. It is observed from Figures 3.11(a) and 3.11(b) that B1 field behavior from MRI and HFSS is similar to a certain extent. Figure 3.12 (a) represent normalized B1 field values on the vertical axis almost passing through the center of the resonator which is also the center of phantom in this case. Similarly, Figure 3.12 (b) represents normalized B1 field values on the horizontal axis. These axes were chosen to plot B1 field data in order to evaluate the same in the center region of the coil, where the small animal is generally placed for an MRI. Figure 3.13 (a) shows that the loaded resonator constructed for MRI and designed in HFSS resonates around the desired Larmor frequency of 127.74 MHz which can be compared, but the input impedance values are not expected to be the same as per reasons mentioned in Section 3.3. It should be noted that S22 was just the name given to the port in QUCS for experimental data, there is only single port excitation associated with the resonator and the name S22 should not be related as S-parameters of any other port. A circular region with 40 mm diameter was chosen at the center of the resonator for quantitative inhomogeneity study. The average normalized B1 from MRI and HFSS

throughout this region was computed to be 0.2995 with a standard deviation of 0.057. Therefore the variation of the B1 field in this region of resonator is about 19%.

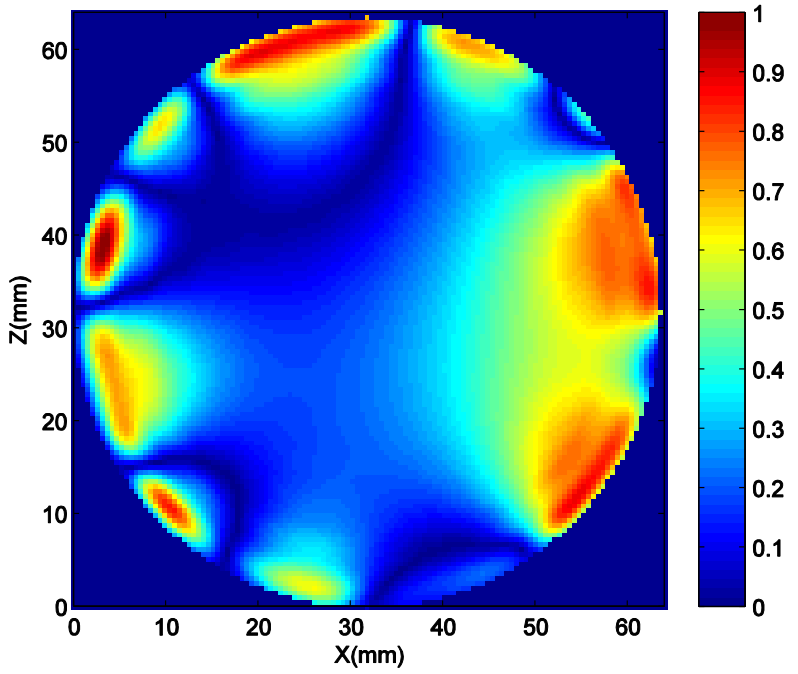

(a)

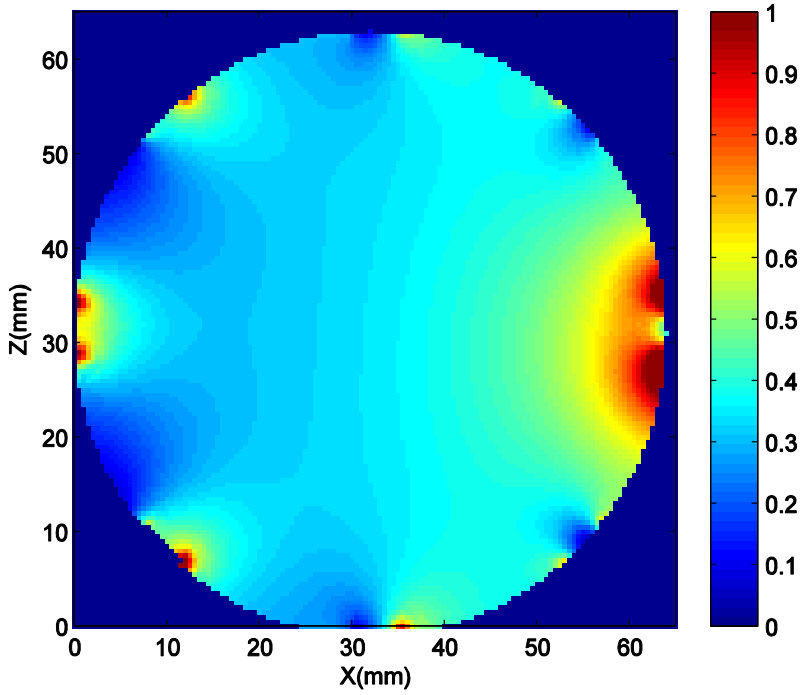

(b)

Figure 3.11: (a) Normalized B1 map generated from MRI (b) Normalized B1 map generated from simulation

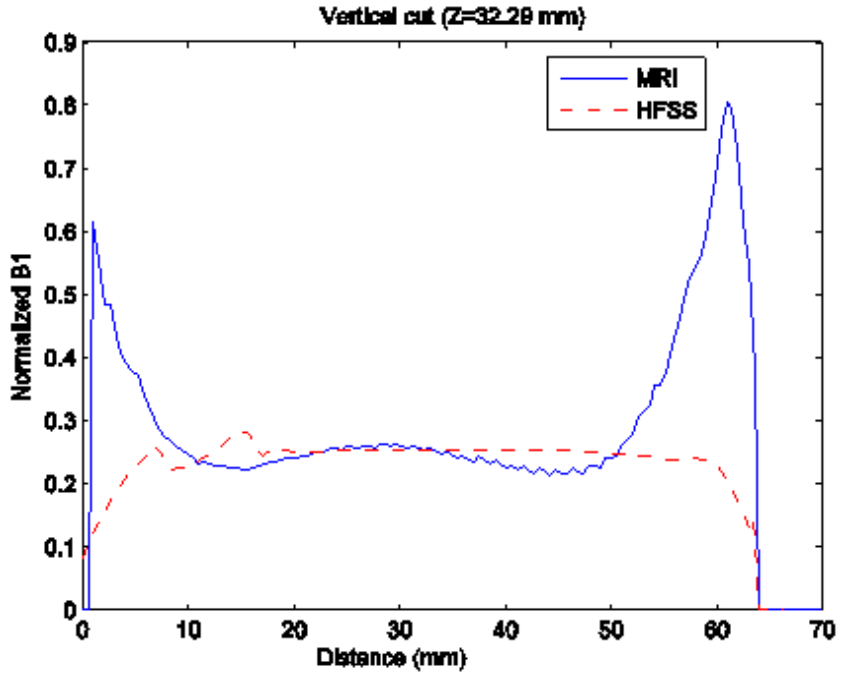

(a)

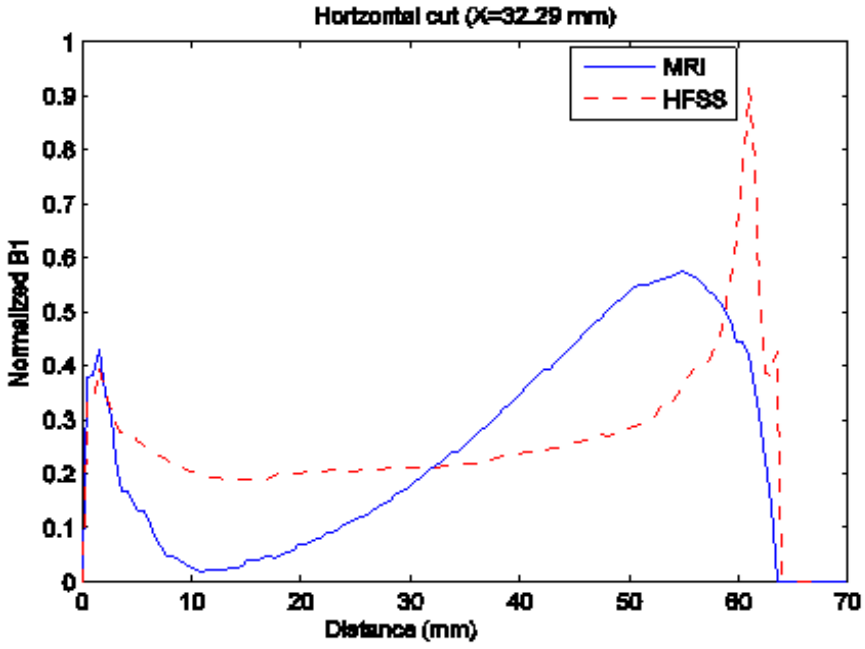

(b)

Figure 3.12: Graphical representation of B1 field data for saline phantom, vertical cut(a) and horizontal cut(b)

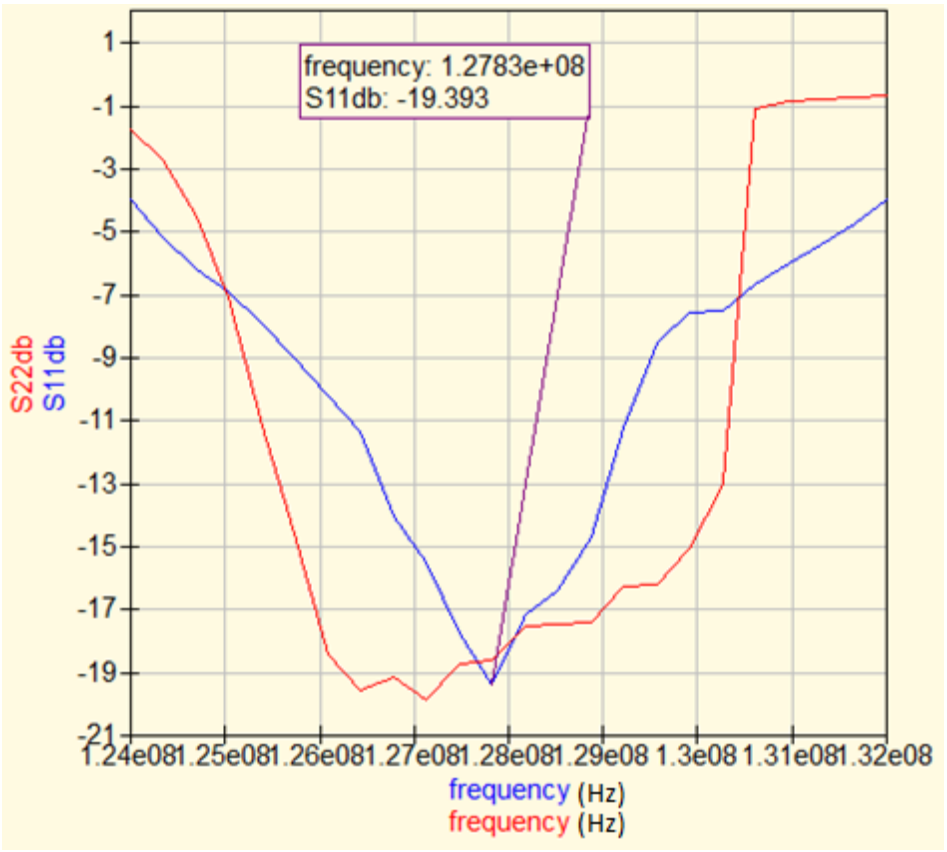

Figure 3.13 (a) : S11 response with saline phantom, simulated (blue) and experimental (red)

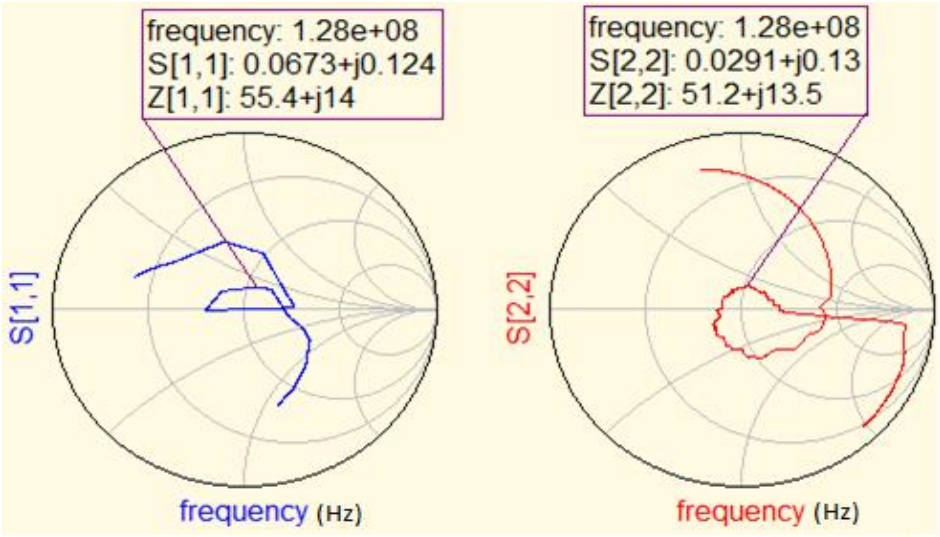

Figure 3.13 (b) : Smith Chart showing input impedance with saline phantom, simulated (blue) and experimental (red)

3.6.3 Discussion

Figures 3.13 (a) and (b) show that the B1 field homogeneity decreases when compared to the mineral oil case. This is also evident from Figures 3.11 (a) and (b). The dark blue rim in Figure 3.14 (a) may be a susceptibility artifact because it arises with the introduction of saline, which in concentration can cause changes in the local B1 field. This artifact could also be due to motion effects [33], meaning movement of the saline solution and the conducting ions inside it. One of the reasons for difference in B1 fields could be exclusion of geometric and material properties of glass. Other reasons for differences in MRI and HFSS generated B1 maps remain the same as discussed in Section 3.5. The difference in Z[1,1] value as compared to QUCS may be due to presence of phantom that absorbs most of the power transmitted by the resonator. The simulation time for this case in HFSS was approximately 5 hours and 55 minutes.

3.7 Complex non-symmetric phantom

3.7.1 Methods for MRI acquisition and MR image processing

A complex non-symmetric phantom was designed by inserting a mineral oil filled glass test tube (capped with a rubber stopper) inside the cylindrical saline bottle to mimic the experimental set up shown in Figure 3.15. The saline phantom remained the same as mentioned in Section 3.6. The details of the mineral oil phantom are mentioned in Table 3.8. The test tube is maintained at a slanting position during experiment and its cross sectional position is modeled in HFSS as shown in Figure 3.15. The complex non-symmetric phantom was utilized to challenge the HFSS simulation by increasing the level of complexity, and hence to validate if FEM based EM field mapping can be used to predict B1 fields inside the birdcage resonator. The MRI B1 map was rotated by 20 degrees to determine B1 field through the mineral oil test tube, so that the vertical slice is taken across it and the results of the same are presented in Appendix A.3. Apart from these, the other methods relating to HFSS simulations and resonance measurement are almost the same as mentioned in Section 3.5.

Table 3.6:- Details of the mineral oil phantom inside saline phantom used for MRI and Simulation

Shape	Dimensions (mm)	Material	Relative permittivity	Relative permeability	Conductivity (S/m)	Temperature in degree Celsius
Cylindrical Test tube	Length = 95 Diameter = 10	Mineral Oil	2.7	1	0	20

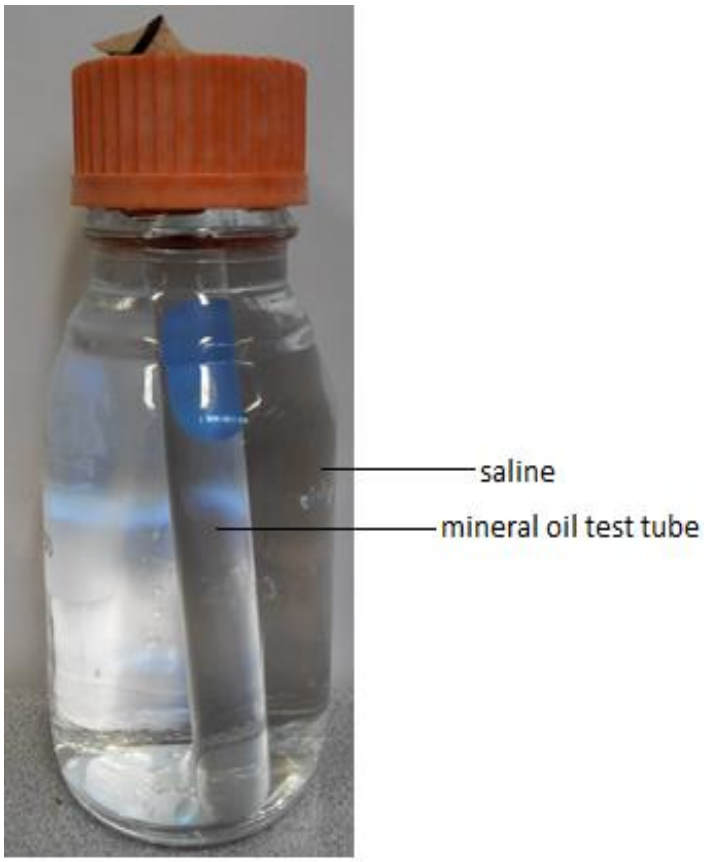

Figure 3.14: The complex non-symmetric phantom

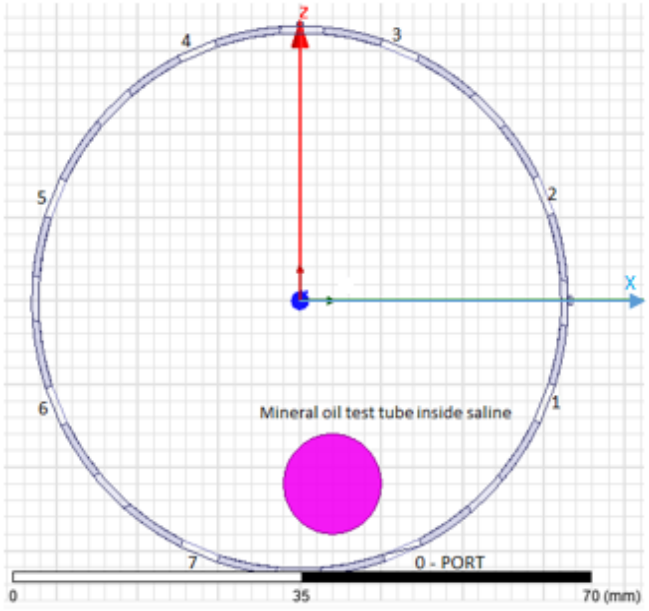

Figure 3.15 : Illustration of the complex non-symmetric phantom constructed in HFSS

3.7.2 Results

Normalized B1 field maps obtained from MRI and HFSS are presented in Figure 3.16 while graphical representation of B1 field data is shown in Figure 3.17. It is observed from Figures 3.16 (a) and 3.16 (b) that B1 field behavior from MRI and HFSS is similar. Figure 3.17 (a) represents normalized B1 field values on the vertical axis almost passing through the center of the resonator which is also the center of phantom in this case. Similarly, Figure 3.17 (b) represents normalized B1 field values on the horizontal axis. These axes were chosen to plot B1 field data in order to evaluate the same in the center region of the coil, where the small animal is generally placed for an MRI. Figure 3.18 (a) shows that the loaded resonator constructed for MRI and designed in HFSS resonates around the desired Larmor frequency of 127.74 MHz which can be compared, but the input impedance values are not expected to be the same as per reasons mentioned in Section 3.3. It should be noted that S22 was just the name given to the port in QUCS for experimental data, there is only single port excitation associated with the resonator and the name S22 should not be related as S-parameters of any other port. A circular region with 40 mm diameter was chosen at the center of the resonator for quantitative inhomogeneity study. The average normalized B1 for MRI and HFSS throughout

this region was computed to be 0.5767 with a standard deviation of 0.057; therefore, the variation of B1 field in this region of resonator is about 10%.

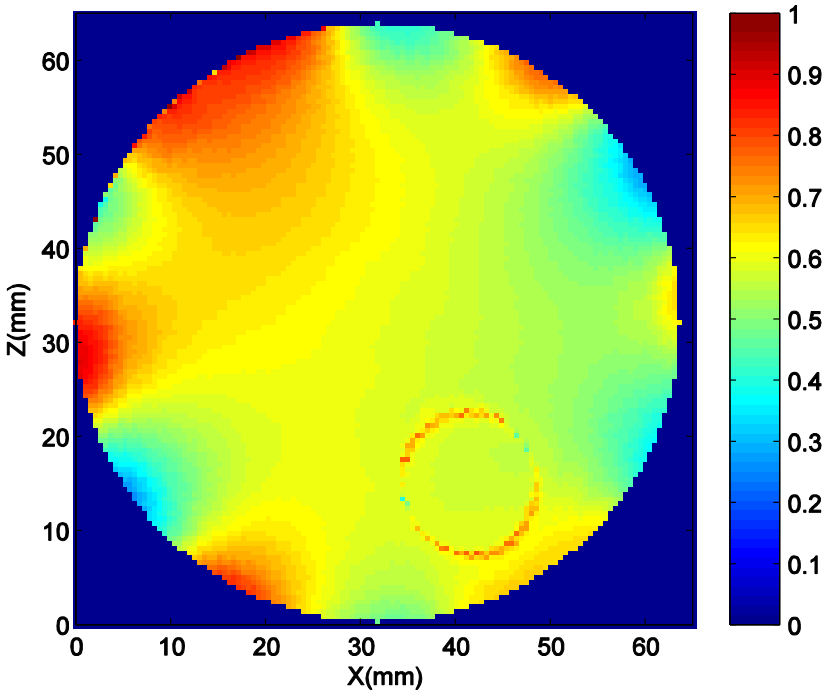

(a)

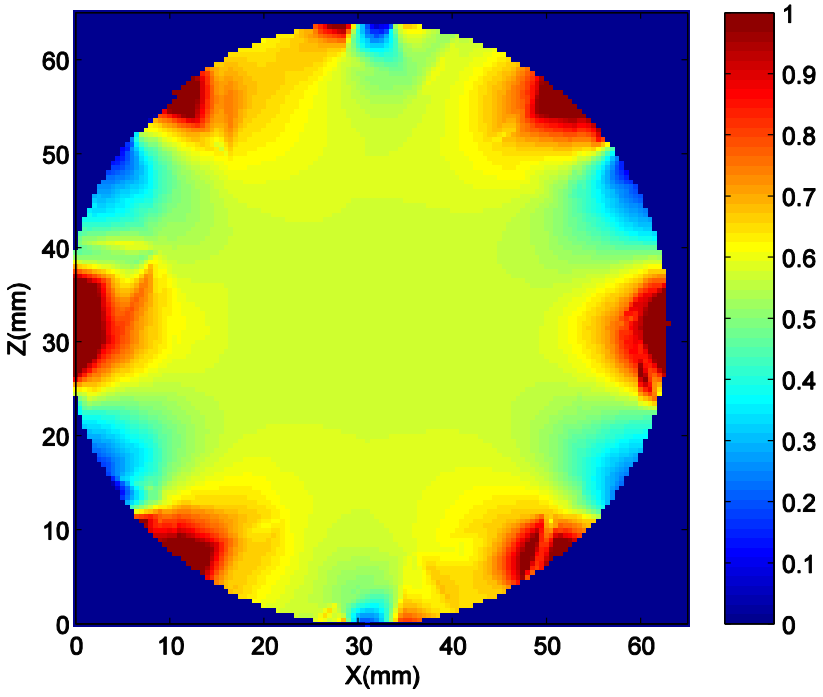

(b)

Figure 3.16: (a) Normalized B1 map generated from MRI (b) Normalized B1 map generated from simulation

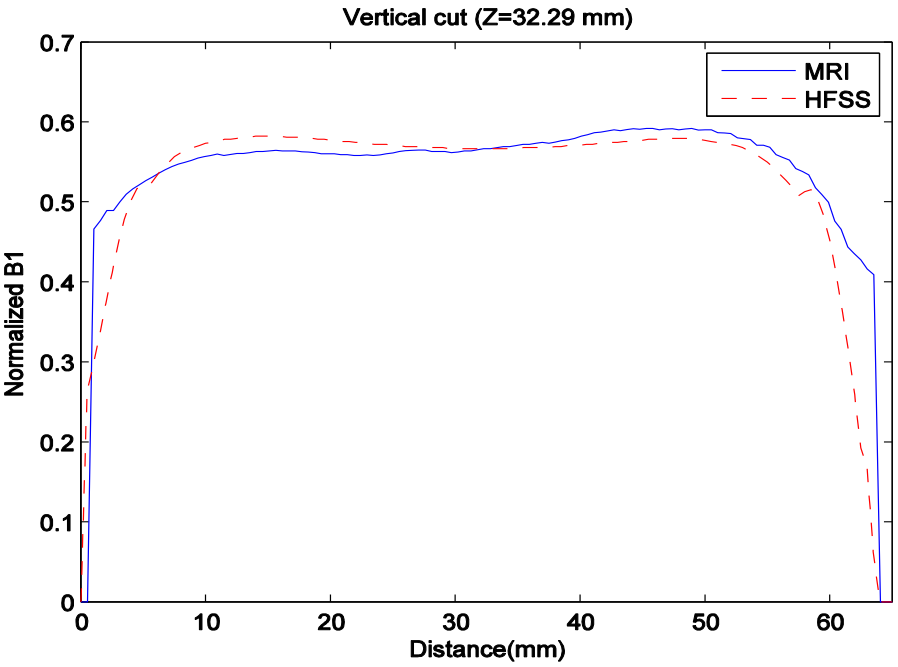

(a)

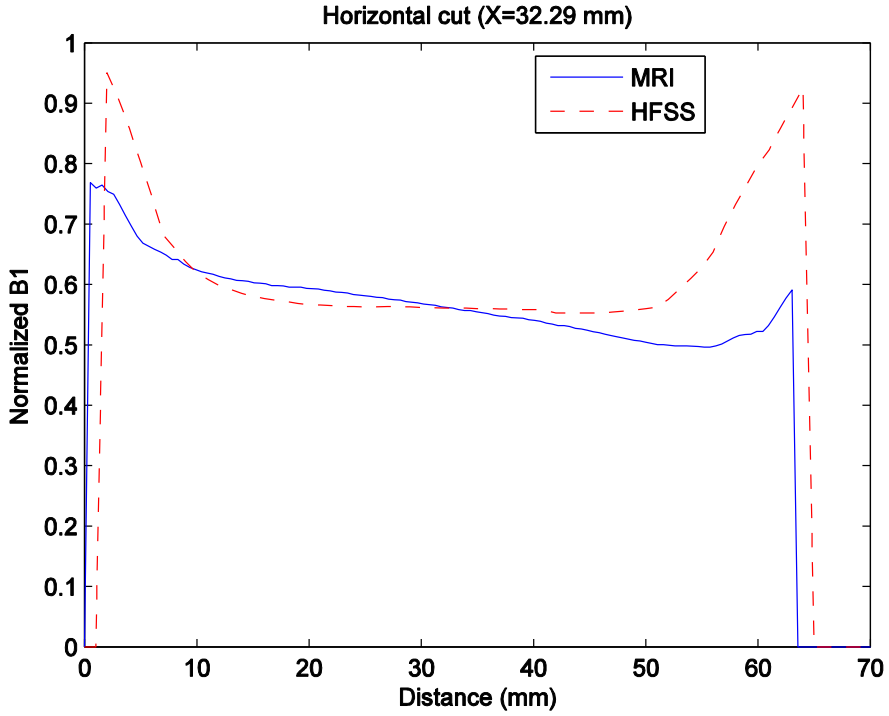

(b)

Figure 3.17: Graphical representation of B1 field data for the complex non symmetric phantom, MRI(a) and Simulation (b)

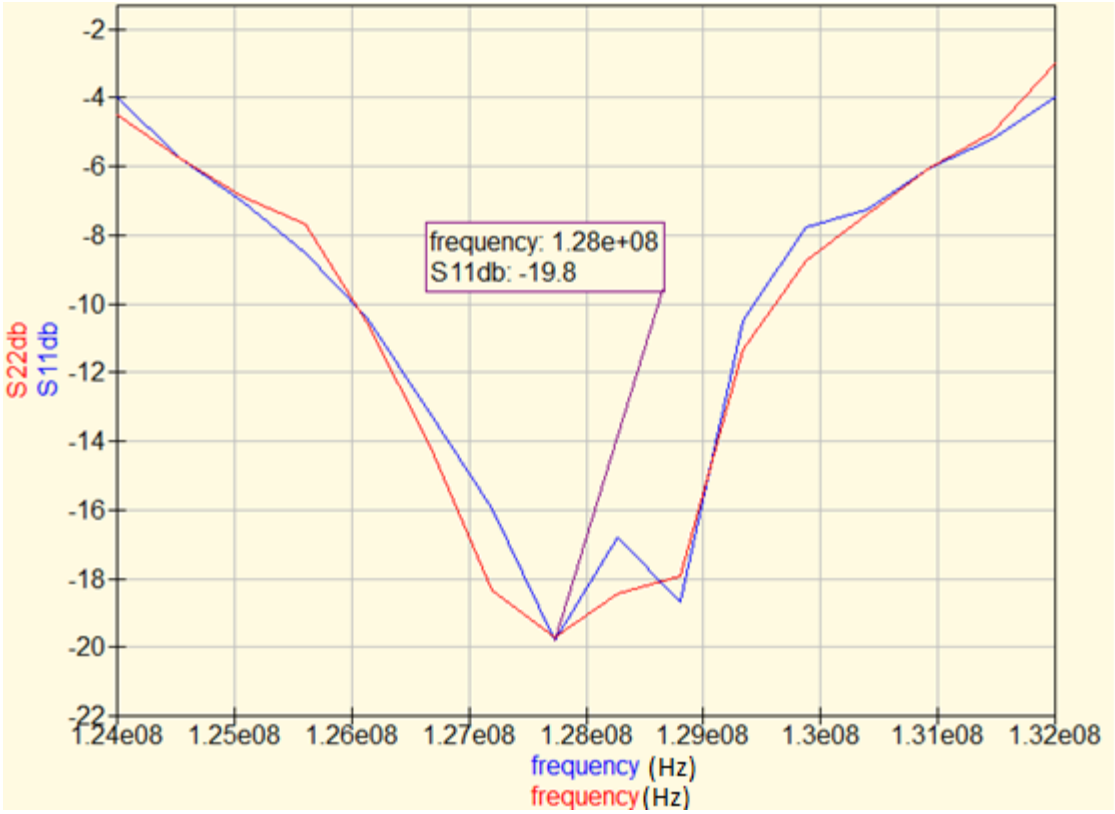

Figure 3.18 (a) : S11 response with complex non-symmetric phantom, simulated (blue) and experimental (red)

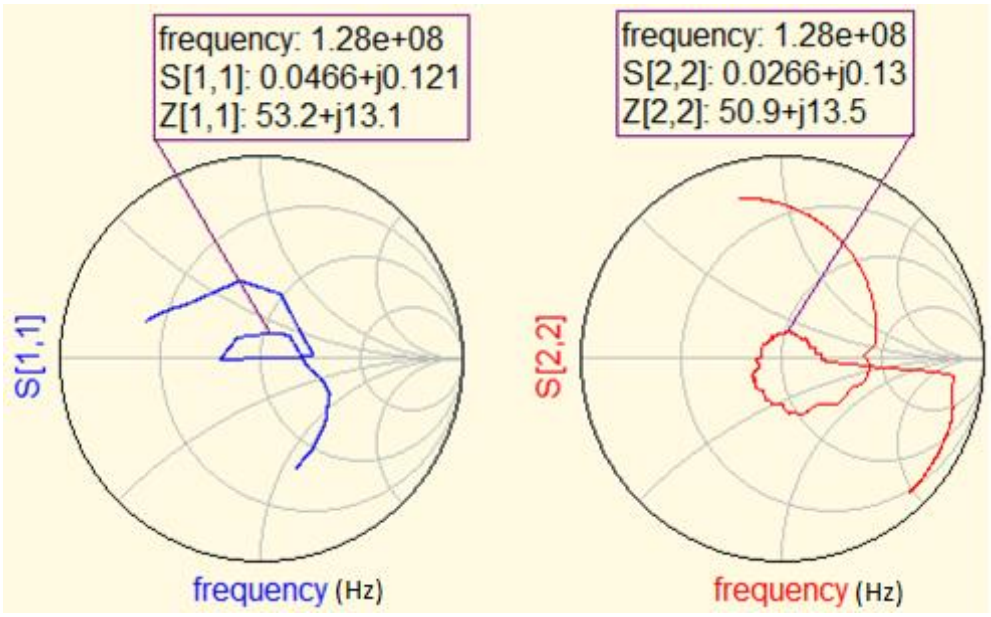

Figure 3.18 (b) : Smith Chart showing input impedance with complex non-symmetric phantom, simulated (blue) and experimental (red)

3.7.3 Discussion

It can be observed from Figures 3.16 and 3.17 that B1 field homogeneity is better in this case when compared to the above two cases of saline and mineral oil phantoms. It is not possible to view the presence of mineral oil test tube in Figure 3.16 (b) due to surface and volume overlap limitations in HFSS. Other reasons for differences in MRI and HFSS generated B1 maps remain the same as discussed in Section 3.5. The simulation time for this case in HFSS considering a completely healed model was approximately 6 hours and 25 minutes.

3.8 Effect of tuning capacitors

Although birdcage resonators are experimentally constructed by iteratively adjusting capacitances to achieve a desired resonant frequency experimentally, the same can be performed in HFSS. Hence simulations were performed in HFSS for the high pass resonator loaded with the same saline phantom for two more commercially available capacitor values in addition to 43 pF to observe the effect of tuning capacitors. The design in HFSS was solved for 47,43 and 39 pF, respectively, to check the tuning, and the results are presented in Table 3.7. The lumped RLC parameter entry in HFSS was used to include the effect of these capacitance values for simulations. The simulations were executed with a frequency sweep of 110 MHz to 150 MHz (step size = 0.01 MHz) with a sparse mesh and lower order basis function to conserve computing resources and simulation time, noting the large frequency range. Hence the results presented in Table 3.7 are fairly generalized and may not apply exactly to practical scenarios for tuning loaded birdcage resonators. It was observed from HFSS simulations that the tuning capacitor value was inversely proportional to the resonance frequency. Simulations suggested that for every pF increase in capacitance the resonance frequency decreased by approximately 3 MHz for the resonator designed and simulated in HFSS.

Table 3.7:- Shift in resonance frequency for different capacitor values

Tuning capacitance (pF)	Resonance frequency(MHz)	S11(dB)
39	139.74	-19.001
43	127.74	-18.012
47	115.74	-18.122

Chapter 4

EM simulation of half birdcage resonator

4.1 Introduction

In this chapter, detailed analysis using the 3D full wave EM simulation of FEM models developed in HFSS of half birdcage resonator is presented. The motivation for this work comes from the fact that full birdcage resonators cannot be positioned in some complex scenarios such as MRI guided high intensity focused ultrasound (HIFU) platforms since they have water underneath the platform which might come in contact with the copper strips. It should be noted that if a birdcage resonator is bisected in a plane which contains the axis of cylindrical symmetry, the resonant modes of the resulting half-birdcage continue to exhibit a standing wave behavior, although now of integral half-wavelengths [21]. The half birdcage resonator presented in Figure 4.1 was designed and constructed by Ms. Kaci Carter (summer student at TBRRI). The construction and tuning procedures of this resonator are similar to the ones mentioned for the full birdcage resonator. Dimensions of the resonator were carefully designed for an optimized filling factor and suitability for small animal imaging experiments keeping in mind the small animal bed and the HIFU platform. In Section 4.2 of this chapter, these models are explained with respect to aspects of FEM like geometry, boundary conditions etc. Then, the EM analyses which is made using the FEM models of half birdcage resonators are discussed in subsequent sections. These are frequency domain analysis which are basically the B1 field solutions inside the half birdcage resonator for a given geometry, solution frequency and capacitance value using FEM.

4.2 Design methodology and simulation set up in HFSS

In this section, half birdcage resonator (structure) developed in HFSS is discussed. We first start with the geometry of the structure. The procedure of modeling the high pass half birdcage resonator in HFSS is analogous to the procedure followed to practically build the half birdcage resonator. The starting point is to set up the design grid in HFSS, in which we first draw a cylinder of required resonator dimensions, after that it is required to cut this cylinder along its

longitudinal axis into two equal halves and further discard one of those. Then the end rings were constructed in such a way so as to accommodate the equal valued capacitors on the top and bottom end rings of this resonator. The picture of the half birdcage resonator is shown in Figure 4.1. The geometry along with a cylindrical saline phantom placed inside the resonator in HFSS is as shown in Figure 4.2. It should be noted that the numbers mentioned in Figure 4.2 are the rung positions.

A 7-rungs half birdcage resonator was designed in HFSS by placing copper strips onto the surface of a machined acrylic tube. Total of six gaps were made on each end-ring to accommodate the tuning capacitors, thus forming a high-pass half birdcage resonator structure. The capacitors were used to tune the half birdcage resonator for the desired Larmor frequency and hence commonly called tuning capacitors. The capacitor values were chosen based on tuning the half birdcage resonator to 127.74 MHz which is the Larmor frequency in consideration. The tuning procedure is one of the critical procedure followed to design the half birdcage resonator and is the same as that of the full birdcage resonator. Once the capacitor values are computed, the full birdcage resonator can be divided into two half birdcage resonators at the zero current position in order to maintain the co-sinusoidal current distribution [21]. The procedure followed for the simulation set up of the half birdcage resonator in HFSS is the same as the one followed for the full birdcage resonator and mentioned in Section 3.3. The RF power fed to the half birdcage resonator was 70 W in HFSS in order to maintain consistency with full birdcage simulations. A frequency sweep was defined in HFSS for the range 122 to 134 MHz to validate the resonance of the half birdcage resonator.

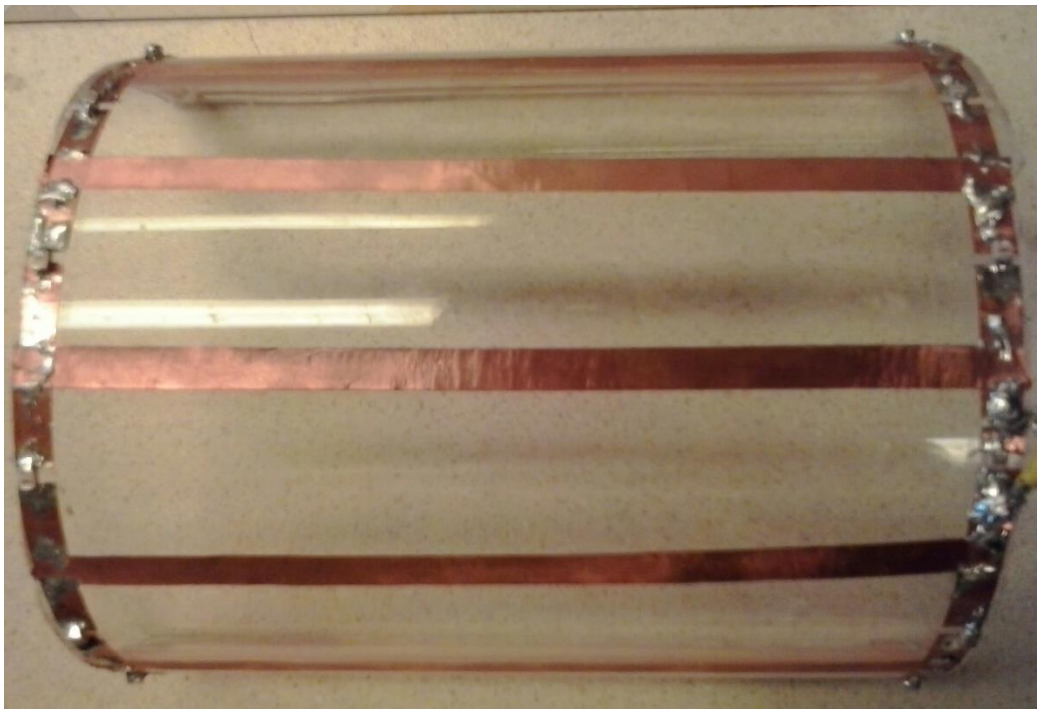

Figure 4.1: Photograph of the half birdcage resonator (top view)

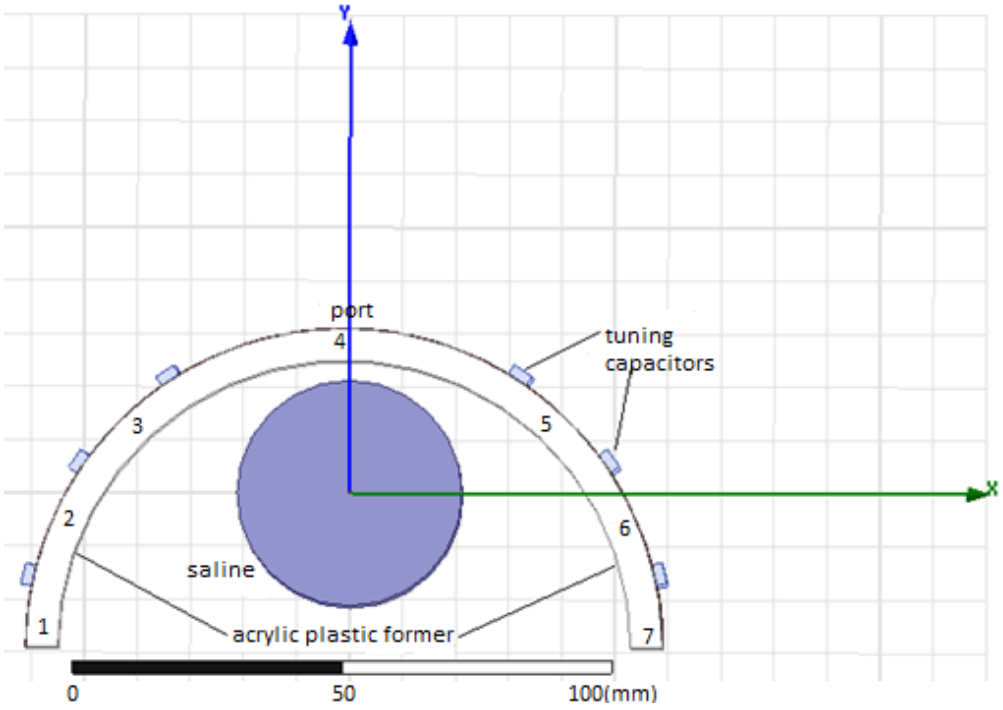

Figure 4.2: A 7 rung high pass half birdcage resonator with cylindrical saline phantom inside (front view) designed in HFSS

Table 4.1: Geometric and simulation details of 7 – rung high pass half birdcage resonator

Diameter (mm)	Resonator length (mm)	Rung length (mm)	Rung width (mm)	End ring width (mm)	Thickness of rungs and rings (mm)	Thickness of frame (mm)	Tuning capacitance (pF)
120	150	135	6.5	6.5	0.06	5	30

Table 4.2: Details of the materials used in EM simulation

Part	Material	Relative permittivity	Relative permeability	Conductivity (Siemens/m)
Resonator frame	Acrylic tube	3.4	1	0
Rings & Rungs	Copper tape	1	1	5.8e7

Table 4.3:- Details of the saline phantom used for simulation

Shape	Dimensions (mm)	Material	Relative permittivity	Relative permeability	Conductivity (S/m)	Temperature in degree Celsius
Cylindrical	Length = 120 Diameter = 42	Saline	81	1	4	20

4.3 Results

Once the design was solved for resonance and B1 field distribution, the B1 field data were exported to Matlab, which was further normalized to maintain consistency with full birdcage B1 maps. The normalized B1 field map generated by the half birdcage resonator inside its volume is presented in Figure 4.3 and its equivalent graphical data are presented in Figure 4.4. The horizontal and vertical axes were chosen in such a way that they pass through the center of the resonator, where the small animal will be placed for MRI. Figure 4.5 displays the S11 response obtained from HFSS simulations, which shows that the half birdcage resonator designed in HFSS resonates at the desired Larmor frequency of 127.74 MHz. The input impedance result is shown in Figure 4.6. and suggests that the resonator has obtained

approximate 50 ohm impedance which suggests that the designed resonator is matched enough to connect it to a MRI scanner for small animal experiments. Impedance matching is necessary in order to minimize power reflection for any RF device. A circular region with 40 mm diameter was chosen at the center of the resonator for quantitative homogeneity study in order to maintain consistency with full birdcage simulations. The average normalized B1 throughout this region was computed to be 0.1999 with a standard deviation of 0.025. Therefore the variation of the B_1 field strength in this region of resonator is about 13%.

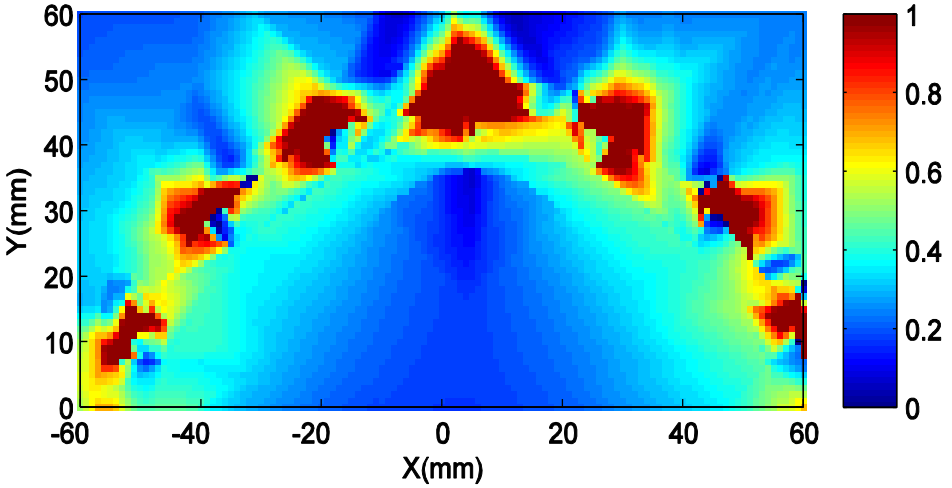

Figure 4.3 Normalized B1 field map inside the half birdcage resonator generated in HFSS and exported to Matlab.

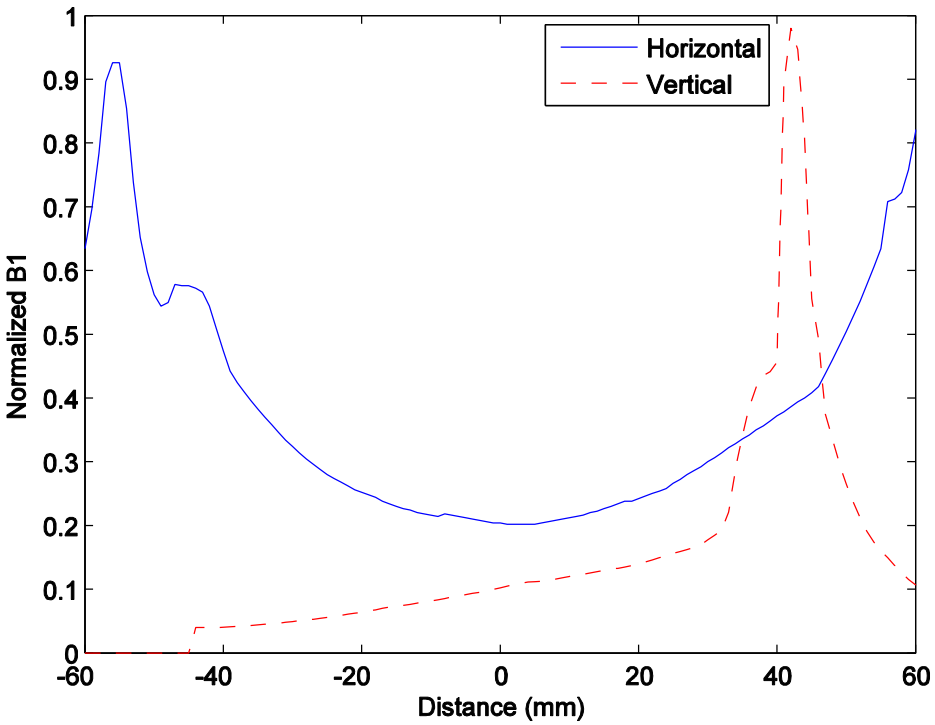

Figure 4.4 Graphical representation of simulated B1 field data inside the half birdcage resonator

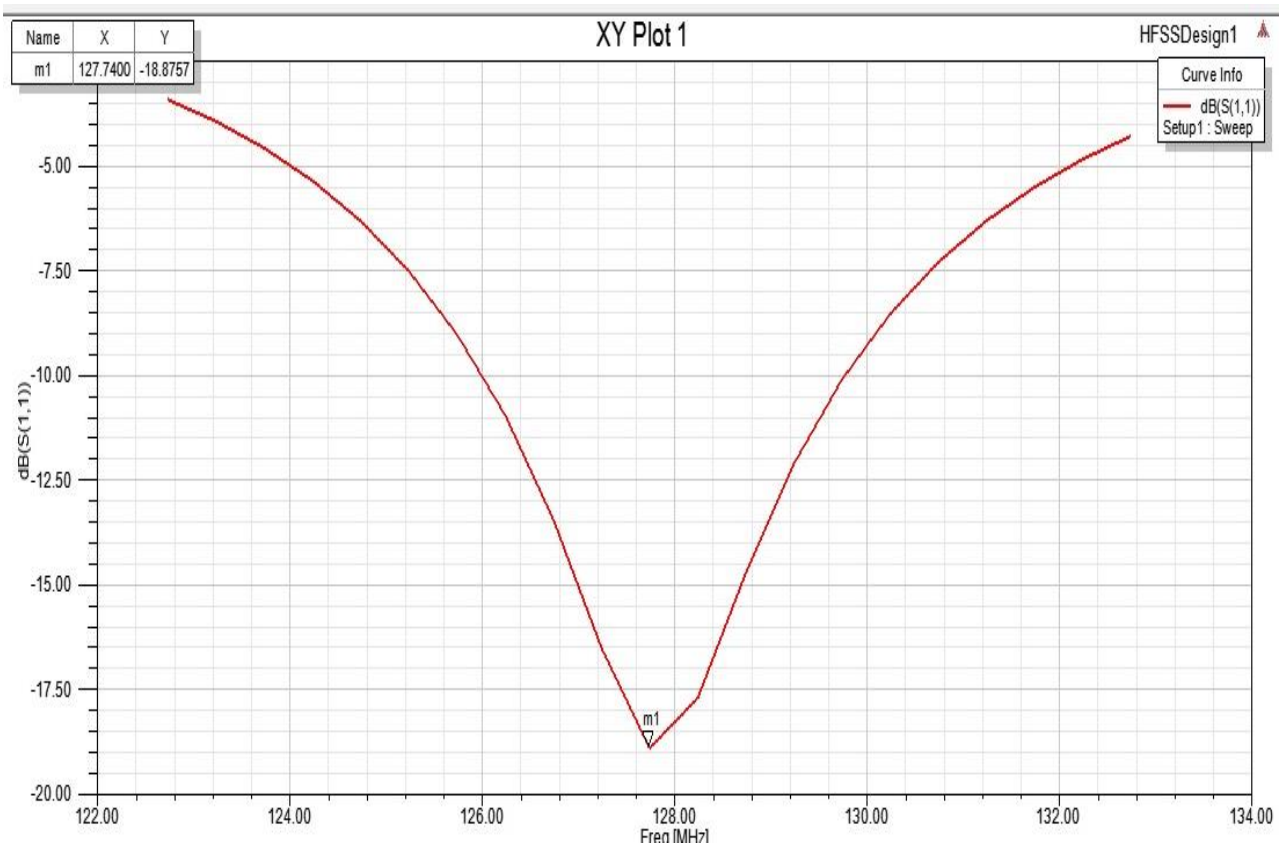

Figure 4.5 Simulated S11 results for half birdcage resonator loaded with saline phantom

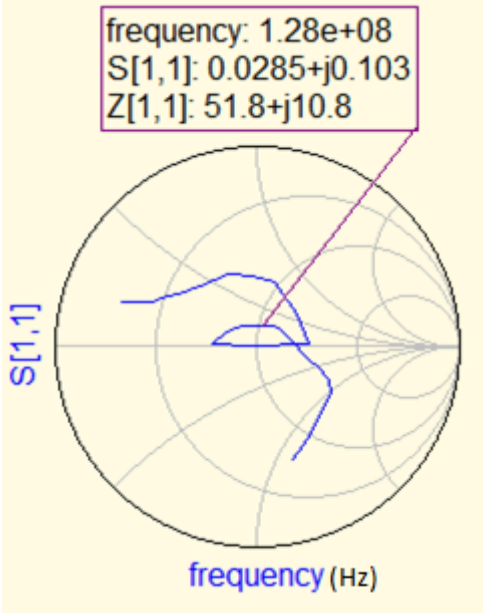

Figure 4.6: Input impedance result for half birdcage resonator

4.4 Discussion

In this chapter the efficiency and performance of half birdcage resonator are evaluated using saline phantom in HFSS. It can be observed from Figure 4.3 that the half birdcage resonator discussed in this chapter is able to generate a fairly homogeneous B1 field inside its volume, especially near the central region of the resonator and hence can be used for small animal MRI. It can be concluded that the half birdcage geometry may provide an alternative to the conventional full birdcage geometry for imaging anatomical regions where use of a full birdcage is difficult due to geometric and positional constraints. For further improvements and future work, geometry of the half birdcage resonator can be optimized by simulating the B1 maps in HFSS, which may be then validated experimentally with the help of MRI B1 maps as done for the full birdcage resonators. Optimizations can allow resonator designers to determine the best design, giving the most homogeneous B1 field in the ROI. As far as boundary conditions are concerned, it should be noted that they are different from the full birdcage case as the presence of air underneath the half birdcage resonator will be one of the reasons for different B1 field distributions between full and half birdcage cases. The simulation time for this case in HFSS considering a completely healed model was approximately 4 hours and 10 minutes.

Chapter 5

Conclusion and future work

5.1 Conclusion

A detailed pre-construction simulation procedure was developed to validate the design and performance of high pass, birdcage and half birdcage resonators taking into consideration the B1 field homogeneity. This procedure was developed for hydrogen nuclei under the primary magnetic field of 3T. The B1 field distribution inside the volume of these resonators is quantitatively evaluated. Experimental and simulation results have thus far shown reasonable agreement in the ROI. The resonator can be tuned to desired Larmor frequency using the simulation environment similar to the procedure followed in practical scenarios. The following conclusions also resulted from this work:

First, while all the simulations run in manageable time, it is clear that if automated optimization of the resonator is required, then the empty resonator or resonator with an ideally homogeneous load would be more suitable to map the B1 field distribution inside the resonator volume in order to get an initial idea of the B1 field distribution. An alternative option to this can be to simulate loaded birdcage resonators in HFSS with the high performance computing (HPC) license of HFSS by running the simulations on multiple central processing units (CPU's) if heterogeneous loading needs to be investigated. Utilizing the HPC license can help in time saving.

Next, exploring 3D full wave FEM based EM simulations can be a useful approach to predict B1 field distributions inside birdcage resonators in terms of saving the valuable resources of time and money by avoiding tedious trial and error techniques employed to tune birdcage resonators to corresponding Larmor frequencies.

Third, since experimental results compare reasonably well with simulation results, FEM based EM simulations may have a reasonable predictive ability to predict EM field distributions inside loaded birdcage resonators.

Fourth, increasing the number of finite elements along with the order of basis functions can deliver more promising results from HFSS as shown in Figure A.2, but this would be at the cost of time and memory.

Finally, it can be concluded that out of all the three cases studied in Chapter 3, B1 field inside the complex non-symmetric phantom has the least variation.

5.2 Future work and potential improvements

The areas of future work identified are as follows:

1. To perform MRI with half birdcage resonator loaded with saline phantom and validate their B1 field maps with the B1 field maps generated in HFSS.
2. To further improve the homogeneity of the birdcage resonators an RF shielding can be designed and simulated in HFSS and then the results of the B1 field distribution can be compared in a similar manner as done in this work, by physically constructing RF shielding around the full and half birdcage resonators.
3. To perform MRI experiments and 3D full wave EM simulations in HFSS for quadrature birdcage resonator designs, meaning birdcage resonators fed with two input ports which are 90 degrees apart electrically.
4. To extend this work to higher frequencies like 171 MHz, 256 MHz etc. as work is actively being carried on birdcage coils to be employed in ultra-high magnetic fields such as 14.1 Tesla [12].
5. To analyze specific absorption rate (SAR) inside loaded birdcage resonators from HFSS simulations. SAR is defined as the RF power absorbed per unit of mass of an object, and is measured in watts per kilogram (W/kg).

Appendix A

A.1 Adaptive meshing in HFSS

The purpose of this appendix is to guide the reader on how the B1 field inside the birdcage resonator can be predicted with an increased accuracy by increasing the number and order of finite elements. The fundamental reason behind increasing the number of finite elements and its order is to generate a more dense mesh inside the birdcage resonator so that abruptly varying B1 field can be mapped. The finite element mesh needs to be locally refined to do this, the procedure that HFSS follows to do this, is termed as 'adaptive meshing' [30,31]. Adaptive meshing is the process of creating an automatic mesh by FEM solvers in EM, which refine the mesh based on previous available solution [31] .

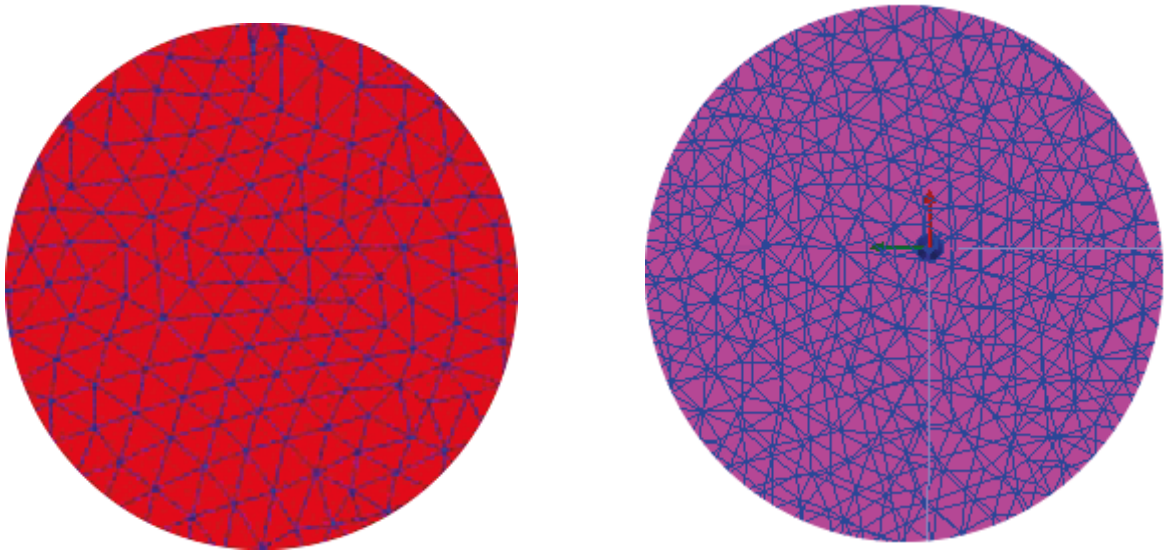

(a) (b)

Figure A.1: Finite element mesh inside birdcage resonator (a) 176512 elements (b) 441912 elements

Figure A.1.(a) shows the finite element mesh with zero order or linear basis functions and with a sparse mesh while Figure A.1.(b) shows finite element mesh with second order or cubic basis functions and with a dense mesh for an 8 rung unloaded birdcage resonator. It should be noted that increasing the number and order of elements in FEM simulation can give experimentally

comparable results similar to the ones presented in this work, but will also amount to computationally intensive resources.

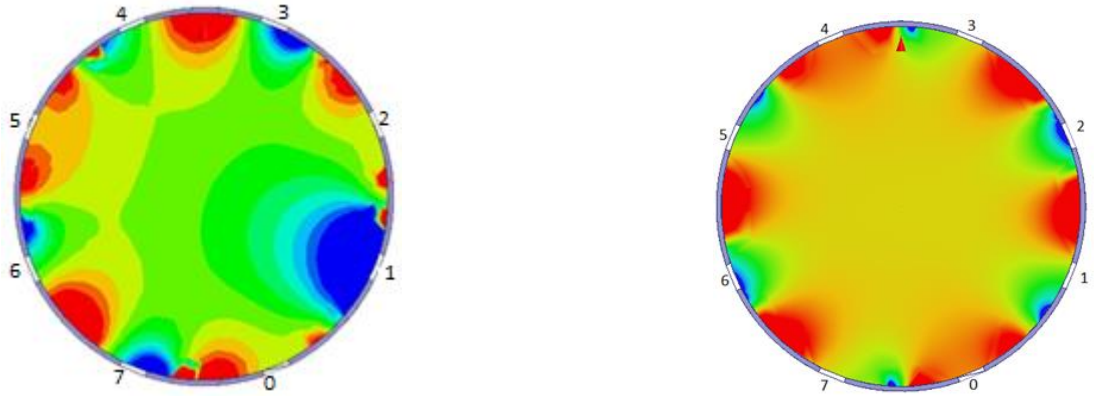

(a) (b)

Figure A.2: (a) B1 field map corresponding to Figure A.1.(a), (b) B1 field map corresponding to Figure A.2.(b)

A.2 Results of HFSS thermal simulation

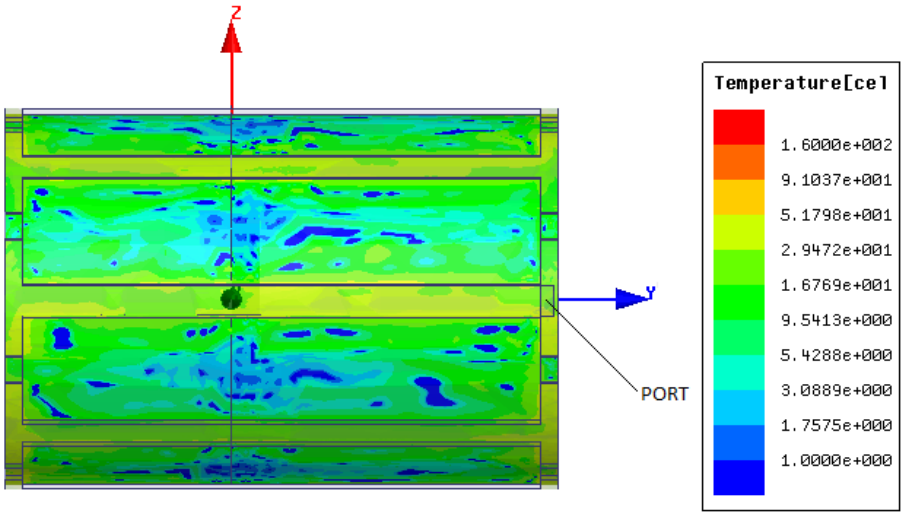

Figure A.3: Temperature profile of the 8 rung high pass birdcage resonator

It can be observed from Figure A.2 that there is no significant temperature rise after the RF input power of 70 W was applied to the resonator in HFSS. The maximum temperature computed was 51.798 ^{o}C . Figure A.2 shows the steady state temperature distribution on the

outer surface of the birdcage resonator, as the copper strip conductors are placed on this surface.

A.3 MRI B1 field results for complex non-symmetric phantom

The purpose of this section is to present the B1 field behavior for the complex non symmetric phantom case for a slice taken through the mineral oil test tube. It is evident from Figure A.3 (a) and (b) that majority of the glass periphery shows high field behavior. This may be due to the material interface.

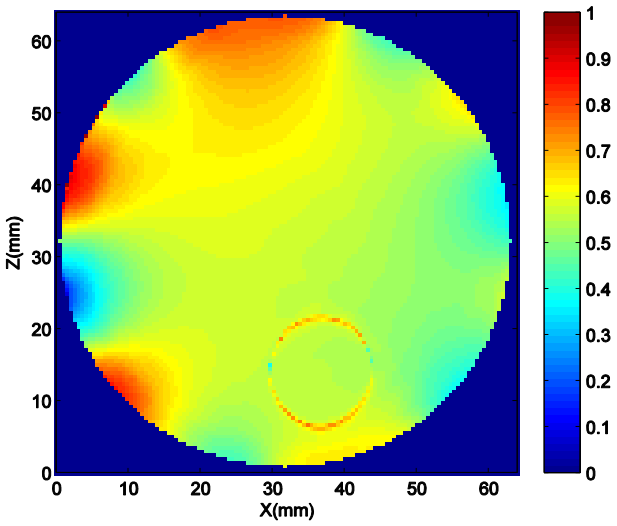

Figure A.4. (a): 20 degrees rotated MRI B1 map with complex non-symmetric phantom

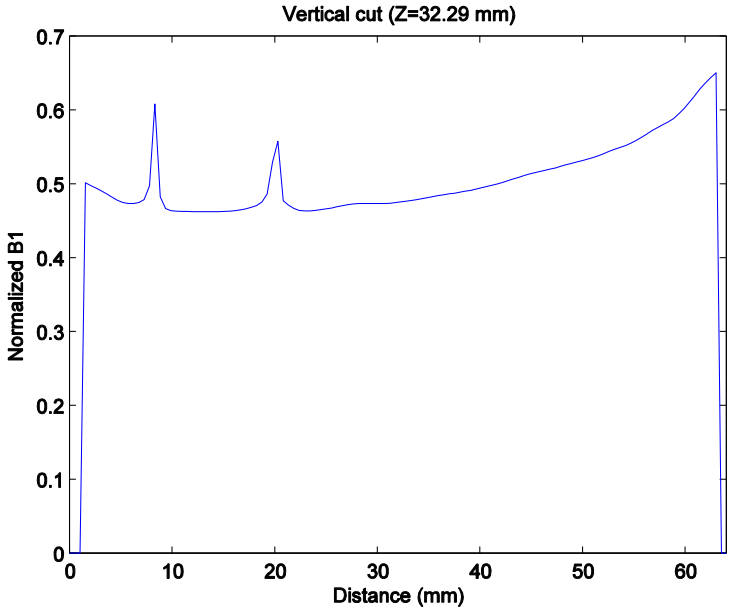

Figure A.4. (b): Graphical representation of B1 field data for Figure A.3. (a)

References

[1] R. H. Caverly “Fundamentals of MRI, IEEE microwave magazine,” July 2015.

[2] E. M. Purcell, H. C. Torrey, and R. V. Pound. Resonance absorption by nuclear magnetic moments in a solid. *Physical Review*, 69:37–38, 1946.

[3] F. Bloch. Nuclear induction. *Physical Review*, 70:460–474, 1946.

[4] P. C. Lauterbur, Image formation by induced local interactions: Examples employing nuclear magnetic resonance. *Nature*, 242:190–191, 1973.

[5] P. Mansfield and P. K. Grannell. NMR ‘diffraction’ in solids? *Journal of Physics C: Solid State Physics*, 6:L422–426, 1973.

[6] R. Pascone, B. Garcia, T. Fitzgerald, T. Vullo, R. Zipagan, and P. Cahill, “Generalized electrical analysis of low-pass and high-pass birdcage resonators,” Magnetic Resonance Imaging, Vol. 9, no. 3, pp. 395 – 408, 1991.

[7] C. E. Hayes et al., “An efficient, highly homogenous radiofrequency resonator for whole-body NMR imaging at 1.5 T,”*Journal of Magnetic Resonance*, (63): 622-628; 1985.

[8] J. Jin, Electromagnetic Analysis and Design in Magnetic Resonance Imaging, CRC Press, 1989

[9] G. Giovannetti, L. Landini, M. Santarelli, and V. Positano, “A fast and accurate simulator for the design of birdcage resonators in MRI,” Magnetic Resonance Materials in Physics, Biology and Medicine, Vol. 15, pp. 36–44, 2002.

[10] T. S. Ibrahim, C. Mitchell, P. Schmalbrock, R. Lee, and D. W. Chakeres, “Electromagnetic perspective on the operation of RF resonators at 1.5 Tesla,” Magnetic Resonance in Medicine, Vol. 54, no. 3, pp. 683–690, 2005

[11] C. Guclu, G. Kashmar, O. Nalcioglu, and A. Hacinliyan, “An FEM approach for the characterization of the RF field homogeneity at high field,” Magnetic Resonance in Medicine, Vol. 37, no. 1, pp. 76–83, 1997.

[12] T. Cheng, A. W. Magill, A. Comment, R. Gruetter, and L. Hongxia, “Ultra-high field birdcage coils: A comparison study at 14.1T,” in *Proc. 36th Annual. Int. Conf. IEEE Engineering Medicine Biology Society*, Aug. 26–30, 2014, pp. 2360–2363.

[13] P. Krenz, “Optimizing MRI coil performance and predicting MRI induced implant heating,” presented at the 2014 ANSYS regional conference Chicago May 23, 2014.
[14] R. H. Hashemi, *et al* ‘MRI The Basics’, Apr 2010.
[15] J. Mispelter, M. Lupu and A. Briguet, “NMR Probeheads for Biophysical and Biomedical Experiments: theoretical principles and practical guidelines”. Imperial College Press, 2006.
[16] C. L. Chin, C. M. Collins, S. Li, B. J. Dardzinski, and M. B. Smith, “Birdcage Builder: Design of specified-geometry birdcage resonators with desired current pattern and resonant frequency,” Concepts in Magnetic Resonance, Vol. 15,no. 2, pp. 156–163, 2002.
[17] A. Deutsch, G. Kopcsay, P. Restle, H. Smith, G. Katopis, W. Becker,P. Coteus, C. Surovic, B. Rubin, J. Dunne, R.P., T. Gallo, K. Jenkins,L. Terman, R. Dennard, G. Sai-Halasz, B. Krauter, and D. Knebel, “When are transmission-line effects important for on-chip interconnections?,” Microwave Theory and Techniques, IEEE Transactions on, Vol. 45, pp. 1836–1846, oct 1997.
[18] C. M. Collins and Z. Wang, “Calculation of Radiofrequency Electromagnetic Fields and Their Effects in MRI of Human Subjects,” Magnetic Resonance in Medicine Vol.65 pp.1470–1482 (2011).
[19] C. M. Collins , S. Li and M. B. Smith, “SAR and B_1 field distributions in a heterogeneous human head model within a birdcage coil,” Magnetic Resonance in Medicine Vol. 40, Issue 6, pages 847–856, December 1998.
[20] M. Alecci, C. M. Collins, M. B. Smith and P. Jezzard, “Radio frequency magnetic field mapping of a 3 Tesla birdcage coil: Experimental and theoretical dependence on sample properties,” Magnetic Resonance in Medicine Vol.46, Issue 2, pages 379–385, August 2001.
[21] D. Ballon, M. C. Graham, S. Miodownik and J. A. Koutcher, “A 64 MHz Half-Birdcage Resonator for Clinical Imaging,” *Journal of Magnetic Resonance*, pp.131-140 (1990).
[22] M. E. Meyerand, *et al* “In Vivo Gradient Echo Microimaging of Rodent Spinal Cord at 7 T,” MRM 40789-791 (1998).
[23] F. Noury, *et al* “MRI methodological development of intervertebral disc degeneration: a rabbit in vivo study at 9.4 T,” Magnetic Resonance Imaging 26 (2008) 1421–1432.

[24] N. Kay and P. Börnert "DREAM—a novel approach for robust, ultrafast, multislice B1 mapping," *Magnetic Resonance in Medicine* 68.5 (2012): pp.1517-1526.

[25] S. Koziel and J. W. Bandler "Space-Mapping Optimization With Adaptive Surrogate Model," IEEE Transactions on Microwave Theory and Techniques, Vol. 55, No.3, March 2007.

[26] R. L. Courant, "Variational Methods for the Solution of Problems of Equilibrium and Vibration," Bulletin of the American Mathematical Society, 49, 1943, pp. 1-23.

[27] S. Ahmed, "Finite-Element Method for Waveguide Problems," Electronics Letters, Vol. 4, No. 18, pp. 387-389, September 1968.

[28] S.R.H. Hoole, Computer Aided Analysis and Design of electromagnetic devices, 1989.

[29] H. Ke and T. H. Hubing, "Low-Frequency Full-Wave Finite Element Modeling Using the LU Recombination Method," ACES Journal, Vol. 23, No. 4, December 2008.

[30] Ansys – HFSS user's manual version 15.0.0

[31] An introduction to HFSS: Fundamental principles, concepts and use, 2009.

[32] J. G. Sled, "Quantitative imaging of magnetization transfer parameters in vivo using MRI," (Doctoral Dissertation, McGill University,2000).

[33] P. Sharma, " Comparison of delayed contrast-enhanced magnetic resonance imaging of myocardial viability at 1.5 and 3 Tesla," (Doctoral Dissertation, Georgia Institute of Technology,2000).

[34] C. H. Cunningham, J. M. Pauly and K. S. Nayak, "Saturated Double-Angle Method for Rapid *B*1+ Mapping," Magnetic Resonance in Medicine 55:1326.